Research article

Tracking glioblastoma progression after initial resection with minimal reaction-diffusion models

Duane C. Harris[1]**, Giancarlo Mignucci-Jiménez**[2]**, Yuan Xu**[2]**, Steffen E. Eikenberry**[1]**, C. Chad Quarles**[2]**, Mark C. Preul**[2]**, Yang Kuang**[1*]**and Eric J. Kostelich**[1*]

[1] School of Mathematical & Statistical Sciences, Arizona State University, Tempe, AZ 85281, USA

[2] Department of Neurosurgery, Barrow Neurological Institute, St. Joseph's Hospital and Medical Center, Phoenix, AZ 85013, USA

* **Correspondence:** Email: kostelich@asu.edu, kuang@asu.edu; Tel: +1-480-965-5006, +1-480-965-6915; Fax: +1-480-965-8119.

Abstract: We describe a preliminary effort to model the growth and progression of glioblastoma multiforme, an aggressive form of primary brain cancer, in patients undergoing treatment for recurrence of tumor following initial surgery and chemoradiation. Two reaction-diffusion models are used: the Fisher-Kolmogorov equation and a 2-population model, developed by the authors, that divides the tumor into actively proliferating and quiescent (or necrotic) cells. The models are simulated on 3-dimensional brain geometries derived from magnetic resonance imaging (MRI) scans provided by the Barrow Neurological Institute. The study consists of 17 clinical time intervals across 10 patients that have been followed in detail, each of whom shows significant progression of tumor over a period of 1 to 3 months on sequential follow up scans. A Taguchi sampling design is implemented to estimate the variability of the predicted tumors to using 144 different choices of model parameters. In 9 cases, model parameters can be identified such that the simulated tumor, using both models, contains at least 40 percent of the volume of the observed tumor. We discuss some potential improvements that can be made to the parameterizations of the models and their initialization.

Keywords: Fisher-Kolmogorov model; glioblastoma multiforme; ensemble prediction; parameter estimation; magnetic resonance imaging; reaction-diffusion equations

1. Introduction

Glioblastoma multiforme (GBM) is the most common and aggressive form of primary brain cancer, with roughly 12,000 cases diagnosed yearly in the United States [1]. Median survival in the U.S. hovers around one year [1] and is not likely to exceed 15 months even with aggressive therapy in

clinical trials [2]. The standard of care for treatment at diagnosis was largely established by the seminal 2005 trial by Stupp *et al.* [2] and consists of maximal safe surgical resection followed by a course of daily oral temozolomide with radiotherapy (chemoradiation), followed by maintenance adjuvant temozolomide. While population-based studies indicate small increases in median survival over recent decades with the advent of more aggressive therapies, including adjuvant chemoradiation and larger tumor resections [1, 3], long-term survival is rare.

GBM inevitably recurs following initial therapy, after which there is no standard of care [4–6]. Although recent advances in the understanding of GBM biology offer the prospect of new and improved treatments [7, 8], patients with recurrent GBM are managed on an individualized basis, according to response to therapy and functional performance status [7, 9]. Treatment options include additional surgical resection; chemotherapy (e.g., temozolomide, lomustine, fotemustine, and irinotecan); and re-irradiation [10]. The use of tumor treating fields, consisting of alternating low-intensity electric fields delivered by transducers applied to the scalp, are supported by several clinical trials [11, 12].

At diagnosis, GBMs typically appear on standard T1-weighted magnetic resonance imaging (MRI) as a bright gadolinium contrast-enhancing tumor rim that correlates with leaky tumor-associated vasculature and proliferating cancer cells. Generally, the rim surrounds a necrotic core with a potentially large edematous T2-hyperintense region extending through otherwise apparently normal brain [13]. It is well established that glioblastomas diffusely invade beyond the contrast-enhancing rim [14].

There have been many efforts over the past three decades to devise mathematical models of the growth of GBM tumors in realistic brain domains. Most models of the gross evolution of GBM tumor growth use a reaction-diffusion equation that is the sum of a diffusion term plus a growth term, which may be exponential or logistic. Murray [15] suggested the Fisher-Kolmogorov (FK) equation, originally proposed in the 1930s to model the spread of genetic traits in a population [16]. The details of this equation are given in Section 2.1.1. The FK equation and variants have been used extensively to perform numerical simulations that capture the growth of gliomas at macroscopic scales; examples include [17–21].

A natural question is the extent to which reaction-diffusion models can predict the progression of GBM tumors. In the simplest case, the solution of the FK model evolves as a propagating front whose velocity is proportional to $\sqrt{D\rho}$, where D is the diffusion rate and ρ is the cellular growth rate. Insofar as the expansion rate of a given GBM tumor potentially can be estimated from a time series of MRI scans, several studies have attempted to determine "patient-specific" model parameters using a variety of methods [19, 21–25]. Murray [25] applied the FK equation with a purely exponential growth term to estimate patient survival times from initial diagnosis. His analysis suggests that tumors with similar overall front velocities but different diffusion-to-growth ratios may have considerably different distributions of tumor cells, which in turn may affect responses to surgical resection and other treatments.

Some recent work has focused on the potential for dynamical PDE models to be applied to the treatment of GBM patients. Hormuth *et al.* [20] incorporated tumor surviving fraction into their calibrated reaction-diffusion model, achieving low error in predictions of tumor response to chemoradiation in a cohort of 9 high-grade glioma patients. Martens *et al.* [21] applied a deep convolutional neural network (DCNN) to multimodal MRI images to reconstruct whole brain cell density distribution and estimate diffusion and proliferation parameters for the reaction-diffusion model. Adequate performance of this approach was demonstrated on synthetic tumors grown over MR brain domains of healthy volunteers

and MR data of a real GBM patient. Lipková *et al.* [26] attempted to combine Bayesian inference and the FK model adapted for structural (MRI) and metabolic (FET-PET) scans to generate personalized radiotherapy plans in 8 cases of GBM that spare more healthy tissue than existing radiotherapy plans.

Efforts to apply a deterministic GBM growth model to clinical data must cope with many uncertainties. Besides the parameters that appear explicitly in the model, the patient brain geometries at the imaging time points must be co-registered (mapped) to each other or to a reference domain. Geometric interpolations may be complicated by the mass effect of the growing tumor [27].

MRI sequences for patients with suspected GBM include T1-weighted sequences before and after gadolinium administration (T1Gd) and T2-weighted fluid-attenuated inversion recovery (T2-FLAIR). Such sequences do not visualize the cancer cells *per se* but rather identify regions of abnormal, leaky vasculature that are associated with the rapid proliferation of tumor cells. In retrospective studies (including this one), often the only readily available data are time series of MRI scans of individual patients and associated records of clinical visits and treatment timelines. Without extensive biopsy data, one must attempt somehow to initialize the model by inferring tumor cell densities from imaging data; such efforts require "segmentations" of patient images into regions corresponding to T1-weighted enhancement and possibly others (such as necrotic core and tumor-associated edema). If one assumes that the diffusivity of GBM cells differs between white and gray matter, then segmentations of those areas must also be defined as part of the computational domain. (Our experience, described in more detail below, suggests that the outputs from automated segmentation tools often vary considerably between patients and within imaging sequences of the same patient.) Treatment artifacts, such as radiation necrosis, may cause regions of MR signal enhancement that resemble those of rapidly growing tumor, a phenomenon called *pseudoprogression* [28]; anti-angiogenic agents can reduce the MR signal and produce a *pseudoresponse* [29].

Finally, even if model parameters could be estimated at a given time point, it seems unlikely that they will stay fixed, as the growth of the tumor waxes and wanes as a consequence of continuing treatment. In summary, uncertainties abound: in the choice of model parameters; the computational domain; the interpretation of MR images; the initial conditions; in quantitative comparisons of model outputs with subsequent patient images; and in the assessment of model errors, as no tractable mathematical model can capture all the relevant details of GBM tumor biology.

The goal of this paper is twofold. First, we introduce a model of GBM growth—which we call the ASU-Barrow (ASUB) model—that may be more biologically realistic than the FK model, which assumes that all GBM cells have the same growth capacity. The ASUB model divides the tumor cell population into two groups: proliferating cells and quiescent (or necrotic) cells. The model is designed to be analytically tractable, efficient to integrate numerically, and to introduce a minimum number of additional parameters. Second, using a retrospective series of 10 patients who all exhibit tumor progression following initial treatment, we investigate whether it is possible to find combinations of parameterizations and initializations that are representative of the range of observed clinical responses to subsequent therapy; both the FK and ASUB models are investigated. Our study is based only on data from MRI sequences that are a routine part of clinical surveillance. All the patients exhibit obvious pathology and have undergone prior surgical resection and continuing and variable treatment protocols. One potential long-term goal of such an effort is to devise a computational tool that could be used as part of efforts to counsel patients about the range of possible outcomes from continued treatment.

2. Materials and methods

2.1. Mathematical models

2.1.1. Fisher-Kolmogorov equation

In this study, we consider two cellular growth models. The first is the Fisher-Kolmogorov (FK) equation, which to our knowledge was first proposed as a way to describe the gross expansion of GBM tumors by Murray [15]. It assumes that tumor cells diffuse linearly (i.e., Fickian diffusion) throughout brain tissue, and that their proliferation at a given location follows a logistic growth trajectory:

$$\frac{\partial n(x,t)}{\partial t} = \nabla \cdot (D(x)\nabla n(x,t)) + \rho(x)n(x,t)\left(1 - \frac{n(x,t)}{K}\right). \tag{2.1}$$

Here $n(x,t)$ represents the cancer cell density at time t and location x. The diffusion coefficient is $D(x)$, which we assume is piecewise constant (possibly greater in white matter than in gray matter). The carrying capacity, K, of the tumor is normalized to 1 for simplicity.

One potential limitation of the Fisher-Kolmogorov model (2.1) is that the model does not consider intratumoral heterogeneity; all cancer cells are assumed to have the same growth and diffusion capability. However, GBM tumors typically outgrow their available blood supply, leaving a rapidly proliferating rim that surrounds a "core" of necrotic or hypoxic cells [14]. Several models have been proposed that divide tumor cells into distinct subpopulations [22, 23, 30–34]. The two-population model used in this paper is described next.

2.1.2. ASU-Barrow model

Han *et al.* [34] proposed a two-population reaction-diffusion model, with proliferating and quiescent (or necrotic) cells that incorporates density-dependent (cross) diffusion. The model can capture the intratumoral heterogeneity and is simple enough that parameter estimation techniques can be applied. However, by introducing a singularity at tumor-free locations, the cross-diffusion terms in this equation complicate the mathematical analysis and make numerical integration computationally expensive (see (2.2)–(2.3) of section 2.1.2). One goal of this work is to present a simplified version of the Han model, which we call the ASUB model, that is computationally inexpensive, amenable to mathematical analysis and parameter estimation techniques, and retains the ability to describe the growth and structure of gliomas.

In the initial model, the tumor is divided into actively proliferating cells, $p(x,t)$, and quiescent cells, $q(x,t)$, with x and t representing location and time, respectively. The quiescent cells are a lumped compartment representing cells that have ceased active division due to competition for space or nutrients, as well as the cells that have undergone necrosis. The model in [34] is given by

$$\frac{\partial p(x,t)}{\partial t} = \nabla \cdot \left[\left(\frac{D_p(x)p(x,t)}{n(x,t)}\right)\nabla n(x,t)\right] + \tilde{g}(n)p(x,t) - \tilde{\delta}(n)p(x,t), \tag{2.2}$$

$$\frac{\partial q(x,t)}{\partial t} = \nabla \cdot \left[\left(\frac{D_q(x)q(x,t)}{n(x,t)}\right)\nabla n(x,t)\right] + \tilde{\delta}(n)p(x,t), \tag{2.3}$$

where

$$n(x,t) = \frac{p(x,t) + q(x,t)}{K}, \tag{2.4}$$

and $D_p(x)$ and $D_q(x)$ are the diffusion coefficients for proliferating and quiescent cells respectively. Proliferating cells grow at the per capita rate $\tilde{g}(n)$ and transition to the quiescent compartment at rate $\tilde{\delta}(n)$. Both rates are monotonic functions of $n(x,t)$, which represents the total cancer cell density, as a fraction of K, at a given location and time. As in the FK model, the carrying capacity, K, of the tumor is normalized to 1 for simplicity.

The functions $\tilde{g}$ and $\tilde{\delta}$ satisfy the requirement that for all $n \in [0, 1]$,

$$\frac{d\tilde{g}(n)}{dn} \leq 0 \qquad \text{and} \qquad \frac{d\tilde{\delta}(n)}{dn} \geq 0, \tag{2.5}$$

with

$$\tilde{g}(0) \geq \tilde{\delta}(0) = 0 \qquad \text{and} \qquad \tilde{\delta}(1) > \tilde{g}(1) = 0. \tag{2.6}$$

In other words, tumor cell growth (death) must be a decreasing (increasing) function of the total cell density. No proliferation occurs at the maximum cell density, and no necrosis occurs at minimal cell density. Similarly to Gyllenberg and Webb (cf. system (2.64) and (2.71) on page 58 of [35]), we implicitly assume that: (1) the necrotic population consists of quiescent and dead cells; (2) the rate at which quiescent cells die is inversely correlated with the nutrient density; and (3) the nutrient density is a decreasing function of the total population n. As a result, the recruitment rate of the necrotic population is a decreasing function of the nutrient density and hence is an increasing function of the total population.

The cross-diffusion terms in Eqs. (2.2)–(2.3) allow the concentration of one cancer cell population to cause a flux in the other. This formulation may be more realistic than simple linear diffusion, where cell populations diffuse independently, and has been employed in previous cancer models [30, 31]. However, the cross-diffusion terms also complicate the mathematical analysis and make the integration of this system computationally expensive. For this reason, we consider the simpler model

$$\frac{\partial p(x,t)}{\partial t} = \nabla \cdot (D(x)\nabla p(x,t)) + \tilde{g}(n)p(x,t) - \tilde{\delta}(n)p(x,t), \tag{2.7}$$

$$\frac{\partial q(x,t)}{\partial t} = \tilde{\delta}(n)p(x,t), \tag{2.8}$$

where $n(x,t)$ is given by Eq. (2.4) and $D(x)$ is the diffusion rate of the proliferating cells. In contrast to the original model (2.2)–(2.3), Eqs. (2.7)–(2.8), which we will call the *ASU-Barrow* (ASUB) model, we assume that proliferating cells diffuse linearly, while quiescent cells do not move (but do take up space). Similar to (2.2)–(2.3), this simpler model emits a traveling wave that can also produce gross growth dynamics that are representative of glioma progression. Although the linear diffusion term $\nabla(D\nabla p)$ implies that only the proliferating cell gradient ∇p drives the invasion process, it does little to recolonize the areas saturated by quiescent cells ($q \gg p, n \approx 1$). The wave solution p component takes the form of a single forward-moving pulsation, and near the tail (where $q \gg p, n \approx 1$) of this formation, the recolonization force pales in comparison to the high death rate at this location.

The model used here defines

$$\tilde{g}(n) = \rho(x)g(n) \qquad \text{and} \qquad \tilde{\delta}(n) = k(x)\delta(n), \tag{2.9}$$

where $\rho(x)$ is the maximum per capita growth rate, $k(x)$ is the maximum death (or quiescence) rate, $g(n) = 1 - B(n; \alpha, \beta)$, and $\delta(n) = B(n; \alpha, \beta)$, where $B(n; \alpha, \beta)$ is the beta cumulative distribution function

(CDF) with shape parameters α and β. To be more precise, we define $B(n; \alpha, \beta)$ such that

$$B(n; \alpha, \beta) = \frac{b(n; \alpha, \beta)}{b(1; \alpha, \beta)}, \tag{2.10}$$

where

$$b(n; \alpha, \beta) = \int_0^n \tau^{\alpha-1}(1 - \tau)^{\beta-1} \, d\tau. \tag{2.11}$$

The beta CDF is chosen because it is a convenient family of functions whose values are between 0 and 1 with extreme values at the endpoints of the unit interval. In this case, $1 - B$ yields a growth coefficient $g(n)$ that is maximal when the total cell density is small ($n \approx 0$) and is zero when $n \approx 1$. By varying the shape parameters, the beta CDF can represent linear, concave up, concave down, or sigmoid proliferation and quiescence responses to changes in the total tumor cell density n. We have chosen $\alpha = 3$ and $\beta = 1$ for the simulations in this paper, as they yield a monotonically decreasing (increasing) and concave down (up) growth (death) term as a function of n, as shown in Figure 1. This choice of g and δ also allows for analytical estimation of D, ρ, and k via the method described in Han *et al.* [34], but other choices may still allow for identifiable parameters [34].
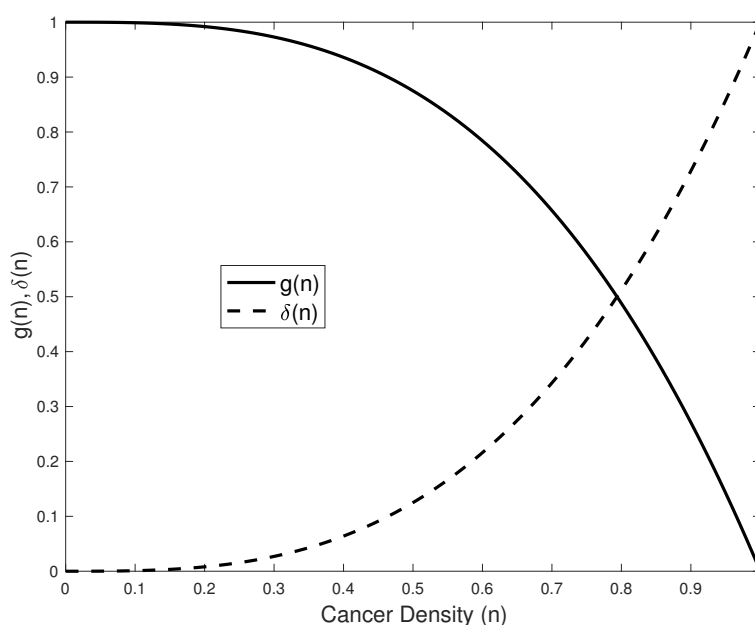

Figure 1. Graphs of the g and δ functions used in the simulations. Here, $g(n) = 1 - B(n, \alpha, \beta)$ and $\delta(n) = B(n, \alpha, \beta)$ where B is the beta CDF with shape parameters $\alpha = 3$ and $\beta = 1$.

2.1.3. Model and initialization parameters

As discussed in the introduction, there are many uncertainties in the initialization of the model as well as in the parameters that appear explicitly within it. In the remainder of this paper, we distinguish between *model parameters*, such as the diffusion and proliferation rates that appear explicitly in the PDE, and *initialization parameters*, which affect the computational domain and choice of initial

conditions from patient MRIs. The model parameters for both the FK and ASUB models include the diffusion coefficient $D(x)$ and the maximum growth rate $\rho(x)$. The ASUB model has one additional parameter, the maximum quiescence rate $k(x)$. The computational implementation allows the values of D, ρ, and k to vary according to the type of brain and tumor tissue: in principle, different values may be chosen accordingly as x represents a voxel corresponding to white matter, gray matter, edematous tissue, necrotic tumor core, or enhancing tumor rim. Some prior studies (e.g., [18,19]) suggest that diffusion rates of GBM cells are faster in white matter than in gray matter. The patients in this study have undergone additional treatment for their recurrences, which in some cases includes the implantation of chemotherapy wafers at the boundary of the resection cavity and re-irradiation of unresected tissue along and near regions that exhibit enhancement on T1Gd MRI scans. For these reasons, we allow for the possibility of differential model parameter values in tumorous regions.

Initialization parameters include choices of initial GBM cell population densities in edematous tissue, along the T1Gd-enhancing rim, and the necrotic tumor core, if present. The classification of tumorous regions can change at every imaging time point, because the tumor is re-segmented and the model is re-initialized from the subsequent MR scans and tissue classification.

2.1.4. Parameter sampling design

Altogether, up to 3 model parameters (diffusion rate D, proliferation rate ρ, and quiescence rate k) must be selected for each of 5 tissue classifications. There are also 3 choices of initialization parameters corresponding to the estimated density of each tumor cell population within each tumorous region (T1-enhancing rim, edema, and necrotic core). Thus, there are potentially $3 \times 5 + 3$ parameters in each simulation of the FK model and $3 \times 5 + 3 \times 2$ parameters for the ASUB model (since initial population thresholds must be selected for two subpopulations). Furthermore, to explore the variability of the simulation results, each parameter must be selected from one of several values (or *levels*) within some reasonable *a priori* range.

Clearly, even for a small number of levels, it is impossible to run simulations over all potential parameters to determine whether some combination produces a result that approximates the evolution of a given patient's tumor. To make the problem tractable, we treat the simulation process as though it were an experimental design and use a so-called Taguchi method [36] to identify sets of parameters that yield a representative range of outcomes using a relatively small number of model runs.

In the Taguchi approach, one first identifies the parameters to which the results are the most sensitive. The values of these parameters are selected independently from a set of *a priori* levels. For example, if the range of the parameters p_1 and p_2 is the interval $[1, 2]$, and there are 5 levels, then p_1 and p_2 may assume any of the values $1.0, 1.25, 1.50, 1.75, 2.0$ in the numerical experiments, and their values are selected independently.

The remaining parameters, to which the results are less sensitive, are grouped into *blocks*, and one chooses from among one of the vectorial combinations; that is, they are not selected independently. For example, if q and r also lie in the interval $[1, 2]$, then one chooses from one of the pairs (q_i, r_i), $i = 1, \ldots, 5$. One can let $q_i = r_i$ or define the pairs in some other way, e.g., $(q_1, r_1) = (1, 2)$, $(q_2, r_2) = (1.25, 1.75), \ldots, (q_5, r_5) = (2, 1)$.

Once the number of levels is fixed, the blocked and independently-chosen parameters are identified, and their values are selected according to an orthogonal array. The approach is a kind of Latin hypercube design. We omit further details, as there is a large literature on the topic; see [36] for one

overview.

2.2. Patient MRI data

2.2.1. Patient cohort and selection

Imaging data of patients who have undergone surgical resection and subsequent treatment at the Barrow Neurological Institute (BNI) were retrospectively analyzed from June 2010 to March 2019. The study's inclusion criteria were the following: age 18 years or older, surgical resection at the BNI, eligibility for standard therapy after surgery, available postoperative MRI consisting of T1-weighted without contrast, T1-weighted with contrast, T2-weighted FLAIR, and sequential progression seen between two MRI scans in either the T1-weighted with contrast or T2-weighted FLAIR sequences. Patients were excluded if excessive motion artifact was present on imaging, at least one MRI sequence was unavailable, the imaging did not show a perceptible progression of disease, or postoperative change and/or radiation necrosis were suspected based on serial imaging. The scans consist of 24 to 30 axial images, extending from the brain stem to the top of the skull, for each patient.

A cohort of 70 patients with histopathologically confirmed glioblastoma multiforme (World Health Organization Grade IV Astrocytoma, GBM) were evaluated. Ten patients met the criteria and were included in the analysis. All patients underwent the standard GBM treatment protocol (i.e., Stupp Protocol) at the BNI and received dexamethasone therapy on the same day of surgical resection. In addition, all patients started radiation therapy with concurrent temozolomide within six weeks of surgical resection. The use of other adjuvant medications (e.g., Afinitor®, Avastin®, Gliadel® wafers, lomustine, Optune®, and procarbazine) were at the discretion of the treating oncologist. Postoperative images were taken at a fixed schedule according to BNI treatment protocol. Images that were taken out of schedule were due either to increase in symptoms or the need for another operation. The study was approved by the St. Joseph's Hospital and Medical Center Institutional Review Board (PHX-19-500-182-20-08).

2.2.2. MRI preprocessing and tumor segmentation

All patient MRIs are preprocessed using a combination of the MATLAB® software package Statistical Parameter Mapping 12 (SPM-12) [37] and the open-source software package 3D Slicer [38]. SPM-12 is used to convert the T1-weighted (with and without contrast) and T2-weighted FLAIR sequences from a DICOM file format into a NIFTI file format. Once converted, 3D Slicer's N4ITK MRI bias-correction tool is used on all sequences to remove any signal inhomogeneity from the MRI data. Then, for each patient, the SPM-12 software is used to co-register all sequences into the native brain space associated with the T1-weighted (without contrast) sequence of the patient's first scan. The resolution of the axial cross-sections was reduced to approximately 256×256, corresponding to a horizontal resolution of 0.75 to 1.0 mm, depending on the patient. (The coarse graining is done by dividing the voxels of each cross-section into 2×2 squares and taking their average as the value for the new grid point.) To keep the method general, default settings were used with all processes. The result in each case is a fully 3-dimensional computational volume consisting of approximately $256 \times 256 \times 25$ voxels. (The number of vertical levels depends on the number of axial images in the first MRI dataset for each patient.) No-flux boundary conditions are imposed wherever brain tissue meets the skull or cerebro-spinal fluid (CSF).

After preprocessing, each tumor voxel is categorized into one of three idealized tissue classifications: necrotic core (hypointense areas on T1-weighted MRI with gadolinium contrast), contrast-enhancing rim (hyperintense on T1-weighted MRI with gadolinium contrast), and tumor-associated edema (hyperintense on T2-FLAIR). For convenience, the names "core," "rim," and "edema" will be used to identify these respective segmentations. To create the segmentations, the NIFTI data is loaded into the 3D Slicer software and the areas that correspond to core, rim, and edema are manually marked using the segmentation tool. These segmentations are performed by experts in neuroanatomy, neuroimaging, and neurosurgery.

Finally, the patient's brain is segmented into tissue types, with each voxel assigned to exactly one of three classes: white matter, gray matter, or CSF. Segmentations are created for each scan via the automatic segmentation tool (with the default settings) provided by SPM-12, using the original (unprocessed) NIFTI file corresponding to the T1-weighted sequence without contrast. Resection cavities are categorized as CSF during this process. The results then undergo the coregistration and resolution reductions described above. All patients of this study have undergone an initial resection of their tumor, and the MRI images are postoperative scans. Consequently, the anatomy of the brain is distorted, and postoperative cavities sometimes are present.

Figure 2 shows a representative 2D cross-section of the 3D computational domain for patient 1. Each panel represents the same slice of a different scan. The number of days since the first scan, t, is written at the upper left of each panel, while the time since the previous scan, Δt, is written at the upper right. The left side of each panel shows the preprocessed T2-weighted sequence with contrast for patient 1, and the right side is the associated brain segmentations. Similar figures can be found for the other patients in the supplementary material (Figures S1–S9).

2.3. Simulation method and error evaluation

2.3.1. Numerical methods

The simulation is initialized using the tumor segmentations described in Section 2.2.2. Each simulation is prescribed density thresholds N_1, N_2, and N_3 (with $0 < N_3 < N_2 < N_1 < 1$) that determine the tumor tissue classifications (i.e., core, rim, and edema) and determine the cell densities for the initial conditions. Voxels that belong to the enhancing rim segmentation are assigned densities between N_2 and N_1, while voxels belonging to the edema segmentation receive densities between N_3 and N_2. Recent studies support the notion that GBM cell density is approximately linearly related to the signal of the T2-FLAIR and T1 weighted (with contrast) sequences [39, 40]. Within a given segmented region, tumor cell densities are vary linearly with respect to MR intensity within the prescribed ranges. (For example, voxels at the maximum intensity within the enhancing rim are assigned an initial cell density of N_1, those of minimum intensity N_2, and linearly in between.) The initialization parameters N_1, N_2, and N_3 are selected according to the Taguchi sampling design outlined in Sections 2.1.4 and 2.3.2.

The initial data for each patient consists of a post-resection MRI. Because most patients in our dataset have had an initial gross total resection, no necrotic tumor core is visible on the initial MRI. The resected tumor tissue has been filled with CSF, and the initial segmentation is labeled accordingly.

For the ASUB model, the tumor is further divided into proliferating and quiescent cells based on the simulation parameters R_1 and R_2, which ascribe an initial percentage of quiescent cells in the rim and edema, respectively. We assume that the rim consists mostly of proliferating cells that are slowly
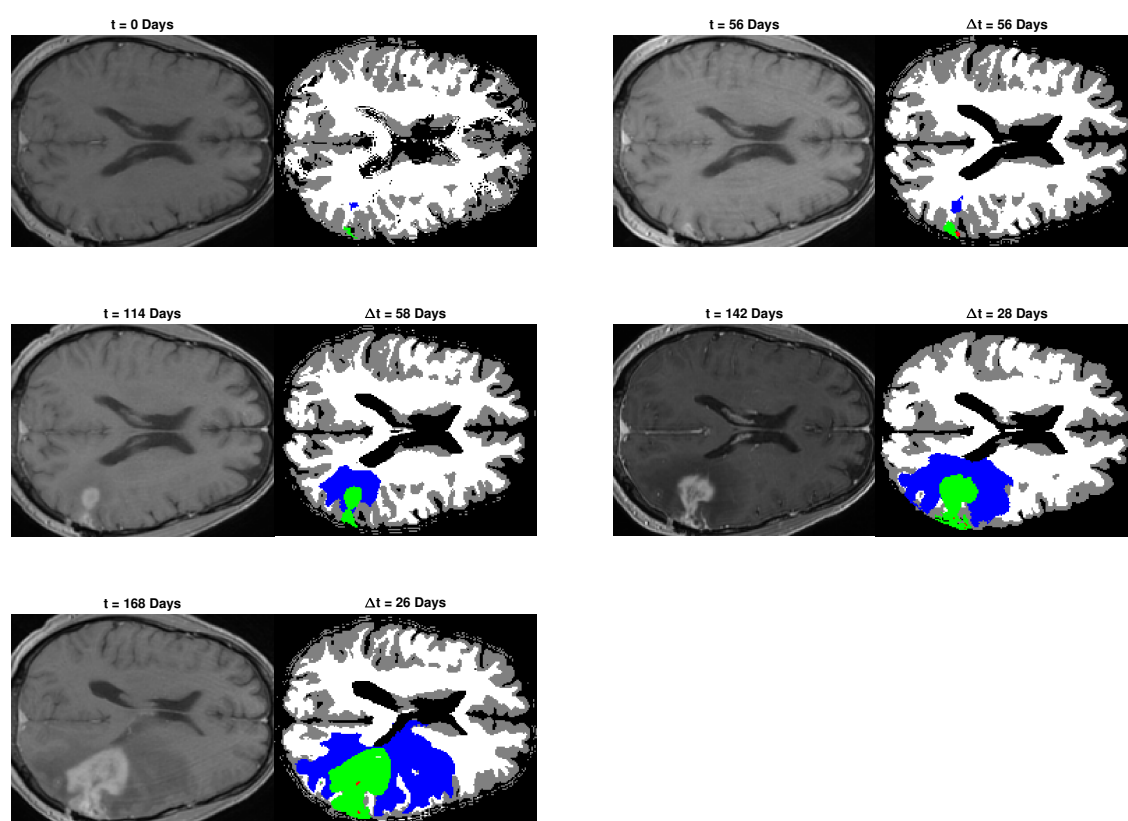
Figure 2. Representative cross-section of MRIs and brain segmentations for Patient 1 at all time points. The number of days since the first MRI (t) and the number of days between MRIs (Δt) is indicated for each scan. Brain segmentations are gray matter (gray), white matter (white), core (red), rim (green), and edema (blue).

infiltrating the edematous regions. We fix $R_1 = 0.0625$ and $R_2 = 0.01$.

Both models are integrated using a Runge-Kutta-Chebyshev (RKC) solver by Shampine *et al.* [41]. RKC methods have been developed especially for reaction-diffusion equations, which tend to yield stiff systems of ordinary differential equations after finite-difference discretization. The diffusion term is integrated explicitly, and the reaction term implicitly. The approach is particularly efficient when the reaction term depends only on the state at a single grid point, which is the case for the models considered here. Given the complex geometry of the brain and the no-flux boundary conditions, the RKC approach is considerably simpler to implement than a fully implicit solver. A multipoint stencil is used to calculate the diffusion term; it avoids the discretization artifacts of a 7-point stencil and allows for larger time steps in an explicit numerical scheme [42]. A 60-day simulation on a typical $256 \times 256 \times 25$ computational domain takes about 30 seconds using one core of an Intel Xeon processor.

Simulations are performed on a three-dimensional brain geometry based on the tissue segmentations described in Section 2.2.2. The spatial resolution varies for each patient but is approximately $0.94 \times 0.94 \times 6.25$ mm with slice thickness having the most variability, ranging between 5 mm and 7.5 mm. We assume that a voxel is part of the tumor core whenever the tumor cell density $n(x, t)$ satisfies $N_1 \leq n(x, t)$, the rim whenever $N_2 \leq n(x, t) < N_1$, and part of the edema whenever $N_3 \leq n(x, t) < N_2$.

All other voxels within the brain interior (i.e., where $n(x, t) \leq N_3$) are labeled as white matter, gray matter, or CSF based on the assignment rendered by SPM-12. Cells proliferate and diffuse through the brain at varying rates as described in Section 2.1.3, while a no-flux condition is imposed at the boundary between brain tissue and CSF.

2.3.2. Simulation ensembles

As noted in the introduction, one objective of this preliminary study is to determine whether we can find sets of model parameters within biologically plausible ranges that can simulate clinically realistic tumors. Of course, neither of the models considered here attempts to incorporate details of GBM biology beyond the gross expansion of the tumor cell population. Our goal is to find model and initialization parameters for which the simulated tumors approximately resemble the clinically observed ones in terms of overall volume (e.g., of T1Gd-enhancing tissue) and approximate location.

The model and initialization parameters form a very large space. Insofar as ours is an exploratory study, we believe that a Taguchi design, as outlined in Section 2.1.4, is appropriate for assessing simulation variability. To simplify the parameter search, we choose $D(x)$ to be a piecewise constant function such that $D(x) = D_1$ whenever x corresponds to a region of white matter or enhancing tumor rim, and and $D(x) = D_2$ elsewhere within the brain. The growth rate is taken to be $\rho(x) = \rho_1$ and the quiescence rate $k(x) = k_1$ when x is in the enhancing rim region, and $\rho(x) = \rho_2$ and $k(x) = k_2$ elsewhere.

One important caveat, and a potential source of simulation error, is that SPM's automated classification of gray and white matter varies considerably between patients and even between scans of the same patient, perhaps because of tumor mass effect and the presence of resection cavities. Manual segmentation of gray- and white-matter tracts has not been possible with the time available to the authors.

Based on analytical and numerical investigations, we expect that the model parameters D_1, D_2, ρ_1, and k_1 and the initialization parameters N_1 and N_2 are the most sensitive; thus, they are allowed to vary independently. Twelve different choices (levels) for each parameter are possible. The possible levels for the white-matter diffusion rate D_1 are twice as large as those for D_2 (cf. Table 1). The levels of proliferation and quiescence rates, ρ_1 and k_1, are chosen independently from the same interval. The cell densities corresponding to enhancing rim are taken from a relatively large interval, given the relatively large variability in the associated MR intensities [39, 40]. The simulation results are less sensitive to choices of the other parameters, which are selected as a block (cf. Table 2). The simulation results include every possible pair of diffusion rates D_1 and D_2 in Table 1.

2.3.3. Error evaluation

Model performance, in terms of predicting tumor evolution from an initial patient MRI to some future scan, is assessed by comparing the simulation results to the actual tumor segmentations. Let S and R denote the set of voxels containing the simulated and real (segmented) tumors respectively, with $|S|$ and $|R|$ being the number of voxels in each. Let $|S \cap R|$ denote the number of voxels occupied by both the simulated and real tumors and $|S \cup R|$, by one or the other. We define the *containment*, C, as the fraction of the simulated tumor that overlaps the real one:

$$C = \frac{|S \cap R|}{|S|}. \tag{2.12}$$

Table 1. Variable parameters and the values used in the simulations. The units of D_1 and D_2 are mm^2 per day, ρ_1 and k_1 are day^{-1}, and N_1 and N_2 are unitless, giving their respective tumor cell densities as a fraction of carrying capacity. Each column defines the interval over which values of the respective parameter are chosen (e.g., $0.2 \leq D_1 \leq 0.4$) and each row indicates one of the 12 possible levels (values) that the parameter may assume in the numerical simulations described here.

Levels	D_1	D_2	ρ_1	k_1	N_1	N_2
1	0.2000	0.1000	0.0038	0.0038	0.3000	0.0600
2	0.2182	0.1091	0.0047	0.0047	0.3500	0.0700
3	0.2364	0.1182	0.0056	0.0056	0.4000	0.0800
4	0.2545	0.1273	0.0068	0.0068	0.4500	0.0900
5	0.2727	0.1364	0.0083	0.0083	0.5000	0.1000
6	0.2909	0.1455	0.0101	0.0101	0.5500	0.1100
7	0.3091	0.1545	0.0122	0.0122	0.6000	0.1200
8	0.3273	0.1636	0.0148	0.0148	0.6500	0.1300
9	0.3455	0.1727	0.0178	0.0178	0.7000	0.1400
10	0.3636	0.1818	0.0217	0.0217	0.7500	0.1600
11	0.3818	0.1909	0.0257	0.0257	0.8000	0.1800
12	0.4000	0.2000	0.0315	0.0315	0.8500	0.2000

The *agreement*, *A*, is defined as

$$A = \frac{|S \cap R|}{|S \cup R|}. \tag{2.13}$$

Suppose for example that the simulated tumor (voxel set S) occupies twice the volume of the actual tumor (voxel set R) as segmented at the comparison time. If the simulated tumor completely contains the actual one, then the containment is 100 percent, but the agreement is only 50 percent. Agreement is a stricter criterion insofar as it measures how well the model predicts the future location of the tumor as well as its volume. The agreement is 100 percent if and only if the simulated and actual tumors occupy the same voxels and is 0 if there is no overlap between them. The definitions imply that $A \leq C$ for every nonempty tumor.

3. Results

3.1. Qualitative results

The results presented here focus on the time intervals when each patient shows the greatest clinical expansion of tumor. The spatial plots are axial cross-sections and represent slices that typically contain the greatest tumor extent, based on the MRI study. (There are 24 to 30 axial cross-sections for each patient in each MRI series.)

Figures 3–5 show representative 2D axial cross-sections, taken from the 3D computational domains created in Section 2.2.2, for Patients 1–3 respectively. (Graphs for the other patients are located in the supplementary material in Figures S10–S16.) For each patient-scan combination in the study, the

Table 2. Block variable parameters and their 12 possible levels. The parameters ρ_2 and k_2 are given per day, and N_3 describes cell density as a fraction of carrying capacity.

Levels	ρ_2	k_2	N_3
1	0.0032	0.0032	0.0100
2	0.0038	0.0038	0.0120
3	0.0047	0.0047	0.0140
4	0.0056	0.0056	0.0160
5	0.0068	0.0068	0.0180
6	0.0083	0.0083	0.0200
7	0.0101	0.0101	0.0220
8	0.0122	0.0122	0.0240
9	0.0148	0.0148	0.0260
10	0.0178	0.0178	0.0280
11	0.0217	0.0217	0.0300
12	0.0257	0.0257	0.0320

ensemble simulations, generated by the method outlined in 2.3.2, are overlaid on top of both the T1-weighted sequence (with contrast) as well as the brain segmentation (cf. Section 2.2.2). To improve the visualization, the edema segmentation has been removed from the brain segmentation and the core segmentation has been combined with the rim segmentation (the core and rim are both green) in these images. The panels on the left-hand side display results generated from the Fisher-Kolmogorov model, Eq. (2.1), and those on the right, the ASUB model, Eqs. (2.7)–(2.8). Each panel shows an axial slice of the T1-weighted, post-contrast MRI on the left and the same cross-section of the computational domain on the right. Panels on the same row correspond to the same scan but different models. For each scan, the time t from the first post-operative scan is shown in the title of the left panel, while the simulation time Δt (the time since the previous scan) is indicated in the title of the right panel.

In each plot, the green curves represent the outer boundary of the rim segmentation at the initial simulation time; the red curves, at the time of the next scan. Each blue curve is a contour line where the total cancer cell density n, as generated by the simulation, is equal to half the maximum value. This is done so that a common metric, which does not depend on specific choices of the free parameters N_1, N_2, and N_3, can be used to compare the experiments. The "50-percent" contour represents a point that is halfway to the wave front, which we believe provides a good representation of tumor densities found in the enhancing rim. Other reasonable choices of the contour lines also are possible (cf. Section 3.2). There are 144 blue curves on each plot, one for each choice of the parameters as described in Section 2.3.2.

The spacing between the contour lines in a region illustrates the sensitivity of the simulation results to the choices of the parameters. Closely spaced contours suggest that many choices of the model and initialization parameters yield comparable results. On the other hand, if only a single contour exists in a location, then the results are sensitive to the choice of one or more model or initialization parameters.
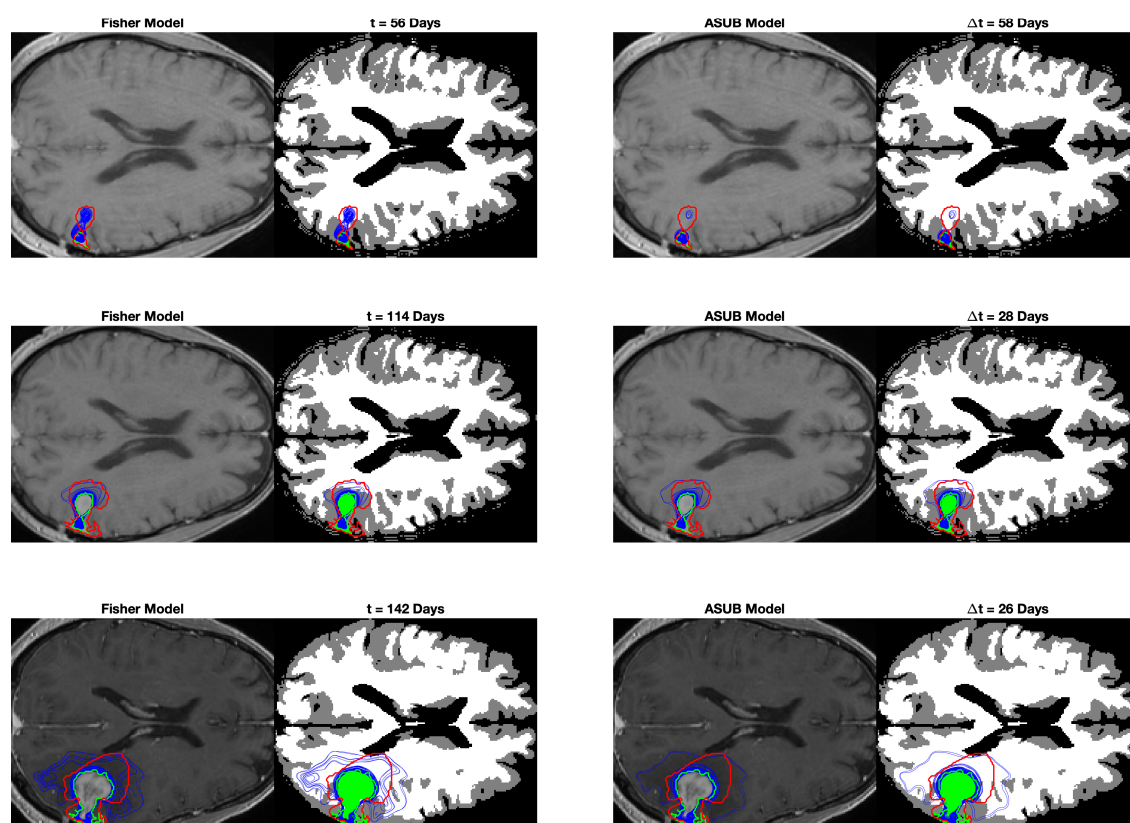
Figure 3. Ensemble of simulations for Patient 1. The panels on the left show solutions from the Fisher-Kolmogorov model, Eq. (2.1), and those on the right, the ASUB model, Eqs. (2.7)–(2.8). The left image in each panel is an axial T1-weighted, post-contrast scan, while the right image is the brain segmentation. The green curves show the outer boundary of the segmentation of the tumor rim, and the red curves likewise but for the subsequent scan. The blue curves show the contour, for each of 144 choices of simulation parameters, where the simulated tumor density is half of the maximum value. They are overlaid on both the scan and the tissue/tumor segmentations that represent the computational domain. The first row of panels shows the patient MRI 56 days following the first post-resection scan; the second row, after 114 days, and the third, 142 days.

3.2. *Quantitative analysis*

We measure both the containment and agreement, Eqs. (2.12)–(2.13), for each set of simulations by comparing the outputs with the tumor segmentations described in Section 2.2.2. In this case, we define R to be the set of voxels that belong to either the rim or core segmentation, and S as the set of voxels such that n is greater than or equal to half the maximum density of the experimental result. In the supplementary material, the containment and agreement results for each patient-scan combination in the study are summarized in Table S1 and Table S2, respectively. For each patient case, the minimum, maximum, and average value and its standard deviation, are reported.

Table 3 shows the average containment and agreement measurements among all simulations. The
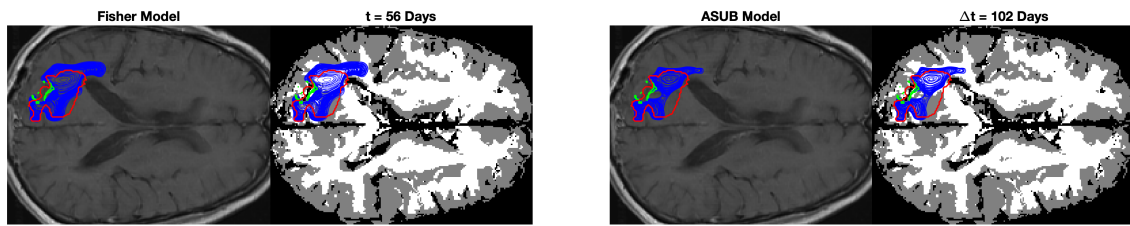
Figure 4. Ensemble simulations for Patient 2. The panels are as in Figure 3.
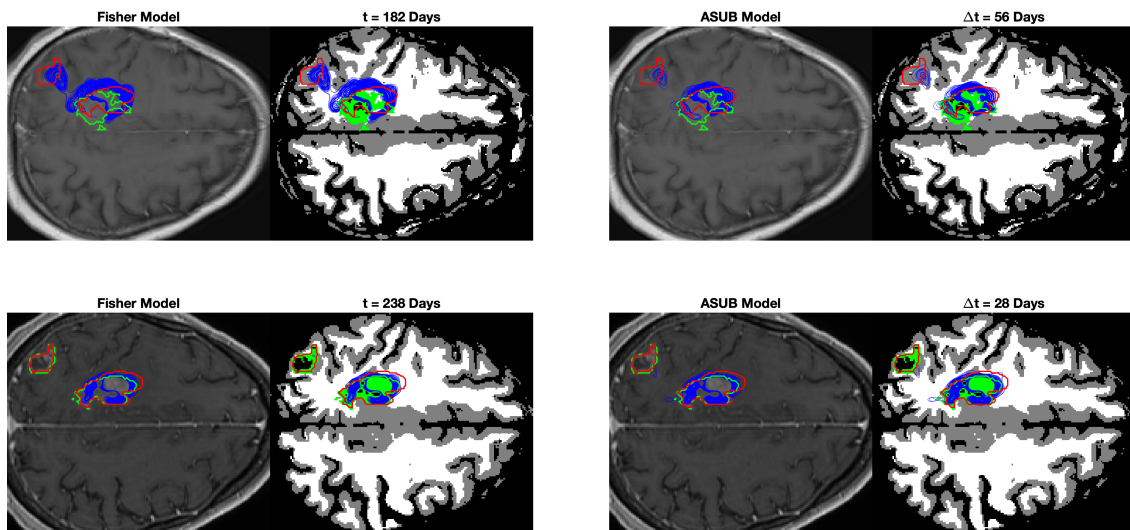
Figure 5. Ensemble simulations for Patient 3. The panels are as in Figure 3.

Table 3. Average containment and agreement for all patient-scan combinations used in the study.

Model	Containment				Agreement			
	Min	Max	Average	Std Dev	Min	Max	Average	Std Dev
Fisher	0.19	0.45	0.29	0.06	0.10	0.29	0.20	0.04
ASUB	0.13	0.46	0.27	0.07	0.09	0.31	0.21	0.05

entries are computed by taking the mean of the appropriate column in Table S1 or Table S2. The same combinations of model and initialization parameters are used for each patient. In some cases, the parameters yield solutions that agree poorly with the observed tumors and correspond to entries in Table 3 that have low containment and agreement scores. The results shown in the "average" columns in Table 3 suggest that the FK model has slightly better containment, while the ASUB model has slightly better agreement with the clinically observed tumors at the next patient-scan time.

Finally, we remark that the results in Table 3 are highly dependent on the choice of contour lines. As noted above, we have chosen the contour lines where the tumor cell density is 50 percent of the carrying

capacity. Other reasonable choices are possible. For example, we can draw the contours corresponding to the maximum tumor cell density in the enhancing rim of the tumor (i.e., N_2, which is an initialization parameter that varies between simulations). Table 4 shows the containment and agreement measures averaged over all patients and over all simulations. The containment values are significantly better and the agreement values are slightly better across the board. However, these contours suggest simulated tumors that are larger in general than the observed ones (see Figures S17–S19 in the supplementary material).

Table 4. Alternative average containment and agreement for all patient-scan combinations used in the study. The results from this table are obtained by using the contours defined by $n = N_2$.

Model	Containment				Agreement			
	Min	Max	Average	Std Dev	Min	Max	Average	Std Dev
Fisher	0.51	0.64	0.59	0.03	0.14	0.25	0.18	0.02
ASUB	0.39	0.64	0.57	0.05	0.15	0.33	0.22	0.04

4. Discussion

In this preliminary study, we have adapted a single-population model based on the Fisher-Kolmogorov equation and a simple two-population reaction-diffusion model (ASUB), Eqs. (2.7)–(2.8), to simulate the gross behavior of proliferating and quiescent (necrotic) tumor cells using clinical MRI scans from patients undergoing treatment for glioblastoma multiforme (GBM). All simulations have been performed using 3D computational domains constructed from individual patients' brain geometries. The simulations attempt to follow the clinical trajectories of 10 individual patients who have undergone either gross total or partial resection of tumor followed by radiation and chemotherapy according to the Stupp protocol [2]. As there is no standard of care for patients who have experienced tumor recurrence, any mathematical model that can predict, with reasonable accuracy, the range of likely progressions would be clinically useful. The results would be useful for patient counseling or for evaluating the therapeutic effect of further treatment, whose benefits must be balanced against potential toxicity and quality of life measures.

For each patient-scan combination, we have generated an ensemble of 144 simulations using a Taguchi design to explore the large parameter space associated with the models and their initializations. Altogether, tumor simulations over 17 different time intervals have been performed, and the results are compared against manual segmentations of tumor imaging performed by neurosurgical experts. All patients who had both imaging evidence of recurrence and biopsy proven recurrence on reoperation were included in the study.

Our results suggest that simple models may be able to provide predictions, with modest skill, of the clinical evolution of recurrent tumors in individual patients over periods of several weeks to months as they undergo a variety of treatments. The performance of the FK and ASUB models is comparable, according to measures of tumor containment and agreement. Of the 17 time intervals studied, parameter sets can be identified in 9 of them such that tumors simulated with the FK and ASUB models contain at least 40 percent of the observed clinical tumor, as defined by Eq. (2.12), and whose overall agreement,

Eq. (2.13), is at least 20 percent for the FK model and 29 percent for the ASUB model (cf. Tables S1 and S2 in the supplementary material).

In several cases, the simulation approach outlined in Section 2.3 yields results in reasonable agreement with the observed subsequent state of the GBM tumor. The results suggest that the it may be possible to determine parameter ranges that yield reasonable simulation results for a variety of patient cases. However, the parameter ranges that produce reasonably good results for Patients 1–3 do not work well for Patients 7 and 10. More work is needed to refine the intervals from which the parameters are selected, and other experimental designs should be considered to assess the sensitivity of the results to a wider range of parameter choices.

One difficulty is the initialization of the models from MRI data, particularly in edematous regions. Although the models often produce a tumor that contains the edematous region, they overestimate the tumor cell density there. Edema occurs as the result of fluid buildup within brain tissue due to a complex combination of leaky tumor-related vasculature, invasion of normal brain tissue by tumor cells, treatment-related effects, and other factors [44]. Edema is associated with tumor recurrence [45] and is treated clinically with dexamethasone [46]. Our models do not attempt to simulate hydrodynamic effects in the brain tissue. In the present simulations, edematous regions are treated simply as areas where tumor cells are present at low levels. Better models of the cellular dynamics in these regions are needed.

Other challenges in the clinical assessment of GBM using MRI include pseudoresponse and pseudoprogression, wherein tumors may appear to shrink or grow, respectively, on surveillance scans, when in fact the results simply are artifacts of treatment [13]. Based on available medical records, all patients included in this study were believed to have experienced actual recurrence at the time of each scan and were treated accordingly, but imaging artifacts due to ongoing treatment cannot be ruled out.

One possible way to make our study more robust would be the use of positron emission tomography (PET) or diffusion-weighted imaging (DWI) to infer tumor cell density. Such imaging techniques have been used in other modeling studies [20, 21, 26], but they are expensive and are not part of standard clinical care. In addition, these studies either did not use pathological subjects, surgical resection was not performed, or areas of hypointensity (i.e., necrosis or resection cavity) were not segmented independently. We believe our study is more clinically relevant and generalizable because it incorporates standard imaging studies and treatment protocols, while also considering the effects of surgery (e.g., resection cavity).

The numerical implementations in this study do not attempt to account for the mass effect of the tumors (i.e., the deformation of the brain anatomy due to the malignant tissue). While finite-element methods can produce realistic depictions of mass effect [17], they complicate the modeling effort; stiffness coefficients for the various brain tissues must be estimated for each patient, among other initialization parameters.

The scans from each patient must be co-registered with one another so that the results of one simulation can be compared with the segmentations at the next scan. In a few cases, the co-registration errors in the vicinity of the segmented tumor are nontrivial (e.g., the agreement between the resection cavities between two successive scans is as low as 75 percent). Such errors decrease the containment and agreement measures even in cases where the model otherwise generates a clinically realistic tumor.

Our simulations do not account for the variability in patient treatment timelines. For example, many of the patients received additional therapeutic treatment that was at the discretion of the oncologist.

Depending on the dose and duration, treatment may affect the clinical progression of the tumor within a given simulation interval. Future work should involve more detailed analyses of treatment timelines with more patients to try to determine, for instance, whether growth and quiescence parameters are significantly affected temporarily by adjuvant therapeutics, and appropriate optimization algorithms should be explored. In addition, future work should include imaging modalities that can estimate the tumor cell density within the tumor (i.e., intratumoral heterogeneity). Inclusion of parameters for cell density will lead to more accurate simulations that agree in directionality.

Finally, we have investigated the potential of a reaction-diffusion equation (the ASUB model) that includes a component for quiescent (or necrotic) cells. The ASUB model appears to perform comparably to the usual FK model, but it introduces another parameter (the cellular quiescence rate), and it takes about twice as long to simulate. On the other hand, the simulations are initialized on patients who have undergone surgical resections that have removed the necrotic core of each tumor, so the ASUB model may not offer an advantage over the simpler FK model for this data set

The analytical approach of Han *et al.* [34] can be adapted to the ASUB model to determine *a priori* parameter estimates in such cases, but we defer such an exploration to future work. Kalman filtering and related data assimilation methods also may be applicable [47, 48], but the analysis of MRI data needs more refinement to account for potential treatment effects. Future work will explore methods to construct observation operators from MRI data and to provide alternative patient-specific estimates of model parameters using Bayesian approaches.

Conflict of interest

The authors declare no conflicts of interest.

References

1. I. W. Pan, S. D. Ferguson, S. Lam, Patient and treatment factors associated with survival among adult glioblastoma patients: A USA population-based study from 2000–2010, *J. Clin. Neurosci.*, **22** (2015), 1575–1581. https://doi.org/10.1016/j.jocn.2015.03.032

2. R. Stupp, W. P. Mason, M. J. Van Den Bent, M. Weller, B. Fisher, M. J. B. Taphoorn, et al., Radiotherapy plus concomitant and adjuvant temozolomide for glioblastoma, *New Engl. J. Med.*, **352** (2005), 987–996. https://doi.org/10.1056/NEJMoa043330

3. M. Eriksson, J. Kahari, A. Vestman, M. Hallmans, M. Johansson, A. T. Bergenheim, et al., Improved treatment of glioblastoma–changes in survival over two decades at a single regional Centre. *Acta Oncol.*, **58** (2019), 334–341. https://doi.org/10.1080/0284186X.2019.1571278

4. M. Weller, T. Cloughesy, J. R. Perry, W. Wick, Standards of care for treatment of recurrent glioblastoma—are we there yet?, *Neuro-Oncology*, **15** (2013), 4–27. https://doi.org/10.1093/neuonc/nos273

5. K. Seystahl, W. Wick, M. Weller, Therapeutic options in recurrent glioblastoma–an update, *Crit. Rev. Oncol. Hemat.*, **99** (2016), 389–408. https://doi.org/10.1016/j.critrevonc.2016.01.018

6. C. Fernandes, A. Costa, L. Osório, R. C. Lago, P. Linhares, B. Carvalho, et al., Current Standards of Care in Glioblastoma Therapy, in *Glioblastoma [Internet]* (ed. S. De Vleeschouwer), Codon Publications, Brisbane (AU), 2017. https://doi.org/10.15586/codon.glioblastoma.2017.ch11

7. S. Lowe, K. P. Bhat, A. Olar, Current clinical management of patients with glioblastoma. *Cancer Rep.*, **2** (2019), e1216. https://doi.org/10.1002/cnr2.1216

8. C. Birzu, P. French, M. Caccese, G. Cerretti, A. Idbaih, V. Zagonel, et al., Recurrent Glioblastoma: From Molecular Landscape to New Treatment Perspectives, *Cancers*, **13** (2021), 47. https://doi.org/10.3390/cancers13010047

9. E. Audureau, A. Chivet, R. Ursu, R. Corns, P. Metellus, G. Noel, et al., Prognostic factors for survival in adult patients with recurrent glioblastoma: A decision-tree-based model, *J. Neuro-Oncol.*, **136** (2018), 565–576. https://doi.org/10.1007/s11060-017-2685-4

10. C. McBain, T. A. Lawrie, E. Rogozińska, A. Kernohan, T. Robinson, S. Jefferies, Treatment options for progression or recurrence of glioblastoma: A network meta-analysis. *Cochrane DB. Syst. Rev. 2021*, **1** (2021), CD013579. https://doi.org/10.1002/14651858.CD013579.pub2

11. R. Stupp, S. Taillibert, A. Kanner, W. Read, D. M. Steinberg, B. Lhermitte, et al., Effect of tumor-treating fields plus maintenance temozolomide vs maintenance temozolomide alone on survival in patients with glioblastoma: a randomized clinical trial, *JAMA*, **318** (2017), 2306–2316. https://doi.org/10.1001/jama.2017.18718

12. O. Rominiyi, A. Vanderlinden, S. J. Clenton, C. Bridgewater, Y. Al-Tamimi, S. J. Collis, Tumor treating fields therapy for glioblastoma: Current advances and future directions, *Brit. J. Cancer*, **124** (2021), 697–709. https://doi.org/10.1038/s41416-020-01136-5

13. D. Yang, Standardized MRI assessment of high-grade glioma response: A review of the essential elements and pitfalls of the RANO criteria. *Neuro-Oncol. Pract.*, **3** (2016), 59–67. https://doi.org/10.1093/nop/npv023

14. O. Eidel, S. Burth, J. O. Neumann, P. J. Kieslich, F. Sahm, C. Jungk, et al., Tumor infiltration in enhancing and non-enhancing parts of glioblastoma: A correlation with histopathology, *PLOS ONE*, **12** (2017), e0169292. https://doi.org/10.1371/journal.pone.0169292

15. J. D. Murray, *Mathematical Biology*, 3rd Edition, Springer-Verlag, 2003. https://doi.org/10.1007/b98869

16. R. A. Fisher, The wave of advance of advantageous genes, *Ann. Eugen.*, **7** (1937), 355–369. https://doi.org/10.1111/j.1469-1809.1937.tb02153.x

17. O. Clatz, M. Sermesant, P. Y. Bondiau, H. Delingette, S. K. Warfield, G. Malandain, et al., Realistic simulation of the 3-D growth of brain tumors in MR images coupling diffusion with biomechanical deformation, *IEEE T. Med. Imaging*, **24** (2005), 1334–1346. https://doi.org/10.1109/TMI.2005.857217

18. C. Hogea, C. Davatzikos, G. Biros, An image-driven parameter estimation problem for a reaction–diffusion glioma growth model with mass effects, *J. Math. Biol.*, **56** (2008), 793-–825. https://doi.org/10.1007/s00285-007-0139-x

19. M. Lê, H. Delingette, J. Kalpathy-Cramer, E. R. Gerstner, T. Batchelor, J. Unkelbach, et al., Bayesian Personalization of Brain Tumor Growth Model, in *Medical Image Computing and Computer-Assisted Intervention – MICCAI 2015* (eds. N. Navab, J. Hornegger, W. Wells, A. Frangi), MICCAI (2015), *Lecture Notes in Computer Science, vol 9350*, Springer, Cham. https://doi.org/10.1007/978-3-319-24571-3_51

20. D. A. Hormuth, K. A. Al Feghali, A. M. Elliott, T. E. Yankeelov, C. Chung, Image-based personalization of computational models for predicting response of high-grade glioma to chemoradiation, *Sci. Rep.*, **11** (2021), 8520. https://doi.org/10.1038/s41598-021-87887-4

21. C. Martens, A. Rovai, D. Bonatto, T. Metens, O. Debeir, C. Decaestecker, et al., Deep Learning for Reaction-Diffusion Glioma Growth Modelling: Towards a Fully Personalized Model?, *arXiv:2111.13404*, (2021). https://doi.org/10.48550/arXiv.2111.13404

22. E. Konukoglu, O. Clatz, B. H. Menze, B. Stieltjes, M. Weber, E. Mandonnet, H. Delingette, N. Ayache, Image Guided Personalization of Reaction-Diffusion Type Tumor Growth Models Using Modified Anisotropic Eikonal Equations, *IEEE T. Med. Imag.*, **29** (2010), 77–95. https://doi.org/10.1109/TMI.2009.2026413

23. I. Rekik, S. Allassonnière, O. Clatz, E. Geremia, E. Stretton, H. Delingette, et al., Tumor growth parameters estimation and source localization from a unique time point: Application to low-grade gliomas, *Comput. Vis. Image Und.*, **117** (2013), 238–249, https://doi.org/10.1016/j.cviu.2012.11.001

24. K. R. Swanson, R. C. Rostomily, E. C. Alvord Jr, A mathematical modelling tool for predicting survival of individual patients following resection of glioblastoma: a proof of principle, *Brit. J. Cancer*, **98** (2008), 113–119. https://doi.org/10.1038/sj.bjc.6604125

25. J. D. Murray, Glioblastoma brain tumours: Estimating the time from brain tumour initiation and resolution of a patient survival anomaly after similar treatment protocols, *J. Biol. Dynam.*, **6** (2012), 118–127. https://doi.org/10.1080/17513758.2012.678392

26. J. Lipková, P. Angelikopoulos, S. Wu, E. Alberts, B. Wiestler, C. Diehl, et al., Personalized Radiotherapy Design for Glioblastoma: Integrating Mathematical Tumor Models, Multimodal Scans, and Bayesian Inference, *IEEE T. Med. Imaging*, **38** (2019), 1875–1884. https://doi.org/10.1109/TMI.2019.2902044

27. T. C. Steed, J. M. Treiber, M. G. Brandel, A. Fotopoulos, S. Voulgaris, M. I. Argyropoulou, Quantification of glioblastoma mass effect by lateral ventricle displacement *Sci. Rep.*, **8** (2018), 2827. https://doi.org/10.1038/s41598-018-21147-w

28. A. Zikou, C. Sioka, G. A. Alexiou, A. Fotopoulos, S. Voulgaris, M. I. Argyropoulou, Radiation Necrosis, Pseudoprogression, Pseudoresponse, and Tumor Recurrence: Imaging Challenges for the Evaluation of Treated Gliomas, *Contrast Media Mol. I.*, **2018** (2018), 6828396. https://doi.org/10.1155/2018/6828396

29. O. D. Arevalo, C. Soto, P. Reblei, A. Kamali, L. Y. Ballester, Y. Esquenazi, et al., Assessment of glioblastoma response in the era of bevacizumab: Longstanding and emergent challenges in the imaging evaluation of pseudoresponse, *Front. Neurol.*, **10** (2019), 460. https://doi.org/10.3389/fneur.2019.00460

30. J. A. Sherratt, Wavefront propagation in a competition equation with a new motility term modelling contact inhibition between cell populations, *Proc. R. Soc. Lond. A.*, **456** (2000), 2365-–2386. https://doi.org/10.1098/rspa.2000.0616

31. J. A. Sherratt, M. A. Chaplain, A new mathematical model for avascular tumour growth, *J. Math. Biol.*, **43** (2001), 291–312. https://doi.org/10.1007/s002850100088

32. K. R. Swanson, R. C. Rockne, J. Claridge, M. A. Chaplain, E. C. Alvord Jr, R. A. Alexander, et al., Quantifying the Role of Angiogenesis in Malignant Progression of Gliomas: In Silico Modeling Integrates Imaging and Histology, *Cancer Res.*, **71** (2011), 7366–7375. https://doi.org/10.1088/0031-9155/57/1/225

33. T. L. Stepien, E. M. Rutter, Y. Kuang, Traveling waves of a go-or-grow model of glioma growth, *SIAM J. Appl. Math.*, **78** (2018), 1778–1801. https://doi.org/10.1137/17M1146257

34. L. Han, S. Eikenberry, C. He, L. Johnson, M. C. Preul, E. J. Kostelich, Y. Kuang, Patient-specific parameter estimates of glioblastoma multiforme growth dynamics from a model with explicit birth and death rates, *Math. Biosci. Eng.*, **16** (2019), 5307–5323. https://doi.org/10.3934/mbe.2019265

35. Y. Kuang, J. D. Nagy, S. E. Eikenberry, *Introduction to Mathematical Oncology*, 1st edition, Chapman and Hall/CRC, 2016. https://doi.org/10.1201/9781315365404

36. R. S Rao, C. G. Kumar, R. S. Prakasham, P. J. Hobbs, The Taguchi methodology as a statistical tool for biotechnological applications: A critical appraisal, *Biotechnol. J.*, **3** (2008), 510–523. https://doi.org/10.1002/biot.200700201

37. W. D. Penny, K. J. Friston, J. T. Ashburner, S. J. Kiebel, T. E. Nichols, Statistical Parametric Mapping: The analysis of Functional Brain Images, 1st edition, Academic Press, London, 2007. https://doi.org/10.1016/B978-0-12-372560-8.X5000-1

38. A. Fedorov, R. Beichel, J. Kalpathy-Cramer, J. Finet, J. C. Fillion-Robin, S. Pujol, et al., 3D Slicer as an image computing platform for the Quantitative Imaging Network, *Magn. Reson. Imaging*, **30** (2012), 1323–1341. https://doi.org/10.1016/j.mri.2012.05.001

39. P. D. Chang, H. R. Malone, S. G. Bowden, D. S. Chow, B. J. A. Gill, T. H. Ung, et al., A multiparametric model for mapping cellularity in glioblastoma using radiographically localized biopsies, *Am. J. Neuroradiol.*, **38** (2017), 890–898. https://doi.org/10.3174/ajnr.A5112

40. E. Gates, J. S. Weinberg, S. S. Prabhu, J. S. Lin, J. Hamilton, J. D. Hazle, et al., Estimating local cellular density in glioma using MR imaging data, *Am. J. Neuroradiol.*, **42** (2021), 102–108. https://doi.org/10.3174/ajnr.A6884

41. L. F. Shampine, B. P. Sommeijer, J. G. Verwer, IRKC: An IMEX solver for stiff diffusion–reaction PDEs, *J. Comput. Appl. Math.*, **196** (2006), 485–497. https://doi.org/10.1016/j.cam.2005.09.014

42. M. Dowle, R. M. Mantel, D. Barkley, Fast simulations of waves in three-dimensional excitable media, *Int. J. Bifurcat. Chaos*, **7** (1997), 2529—2545. https://doi.org/10.1142/S0218127497001692

43. H. Akaike, A new look at the statistical model identification, *IEEE T. Automat. Contr.*, **19** (1974), 716-723. https://doi.org/10.1109/TAC.1974.1100705

44. Z. X. Lin, Glioma-related edema: New insight into molecular mechanisms and their clinical implications, *Chin. J. Cancer*, **32** (2013), 49–52. https://doi.org/10.5732/cjc.012.10242

45. X. Qin, R. Liu, F. Akter, L. Qin, Q. Xie, Y. Li, et al., Peri-tumoral brain edema associated with glioblastoma correlates with tumor recurrence, *J. Cancer*, **12** (2021), 2073–2082. https://doi.org/10.7150/jca.53198

46. M. Cenciarini, M. Valentino, S. Belia, L. Sforna, P. Rosa, S. Ronchetti, et al., Dexamethasone in glioblastoma multiforme therapy: Mechanisms and controversies, *Front. Mol. Neurosc.*, **12** (2019). https://doi.org/10.3389/fnmol.2019.00065

47. E. J. Kostelich, Y. Kuang, J. M. McDaniel, N. Z. Moore, N. L. Martirosyan, et al., Accurate state estimation from uncertain data and models: An application of data assimilation to mathematical models of human brain tumors, *Biol. Direct*, **6** (2011), 64. https://doi.org/10.1186/1745-6150-6-64

48. J. McDaniel, E. Kostelich, Y. Kuang, J. Nagy, M. C. Preul, N. Z. Moore, et al., Data Assimilation in Brain Tumor Models, in *Mathematical Methods and Models in Biomedicine* (eds. U. Ledzewicz, H. Schättler, A. Friedman, E. Kashdan), Springer, New York, NY, 2013, 233–262. https://doi.org/10.1007/978-1-4614-4178-6_9

Supplementary material

Tissue/Tumor segmentations
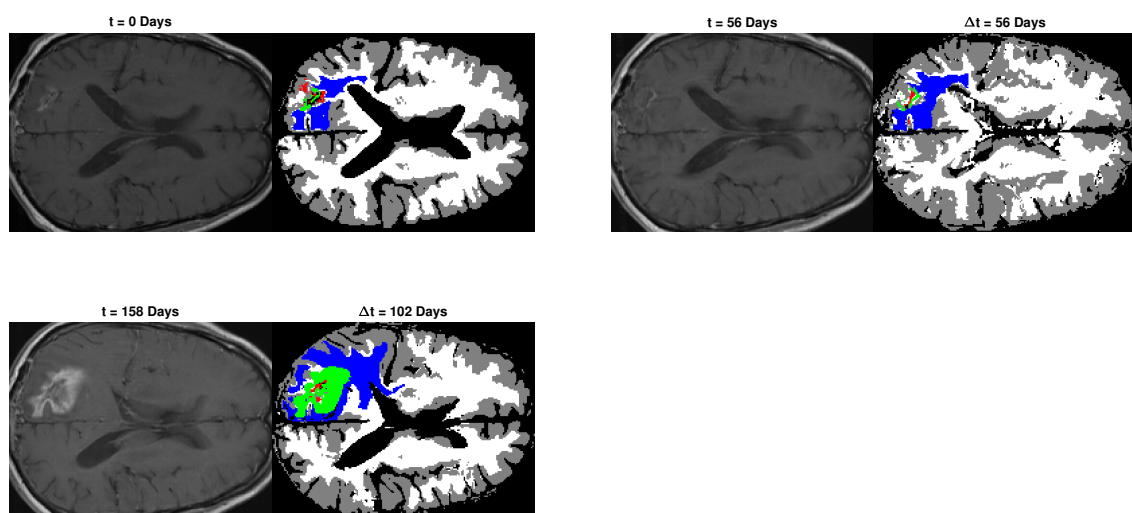
Figure S1. Representative cross-section of MRIs and tumor segmentations for patient 2 at all time points. The panels are as in Figure 2.
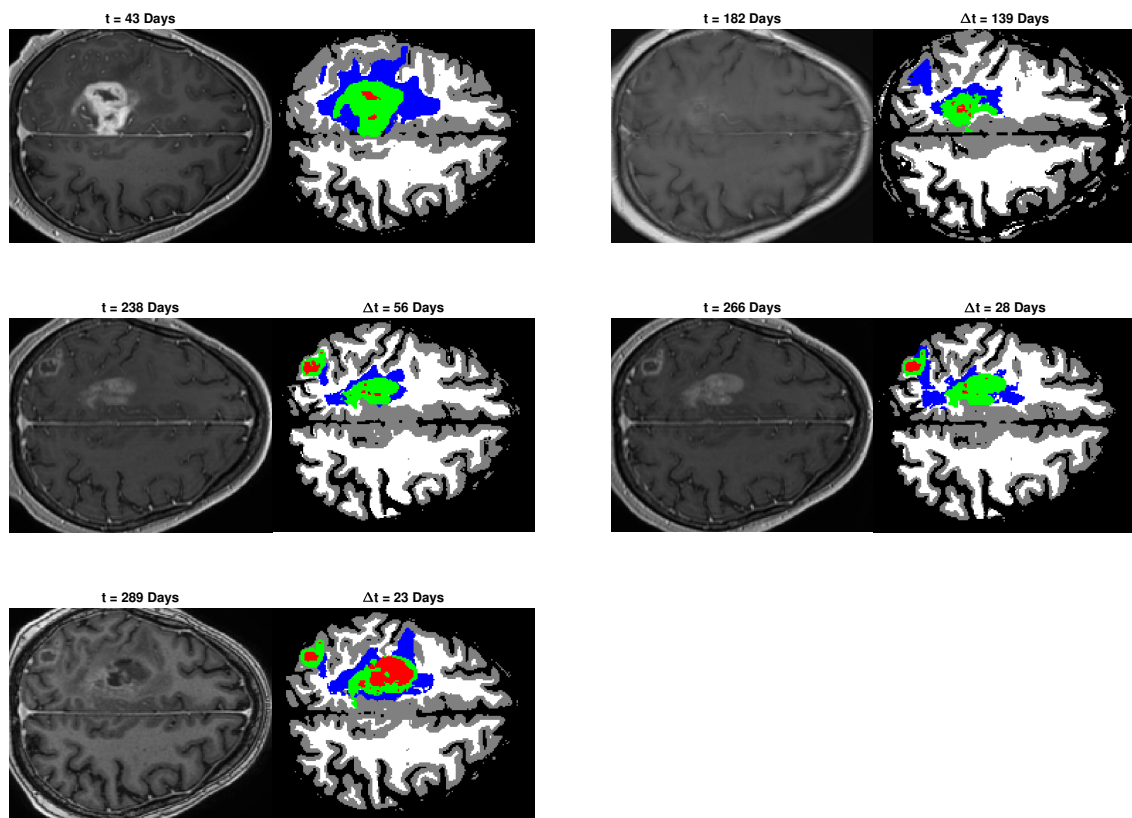
Figure S2. Representative cross-section of MRIs and tumor segmentations for patient 3 at all time points. The panels are as in Figure 2.
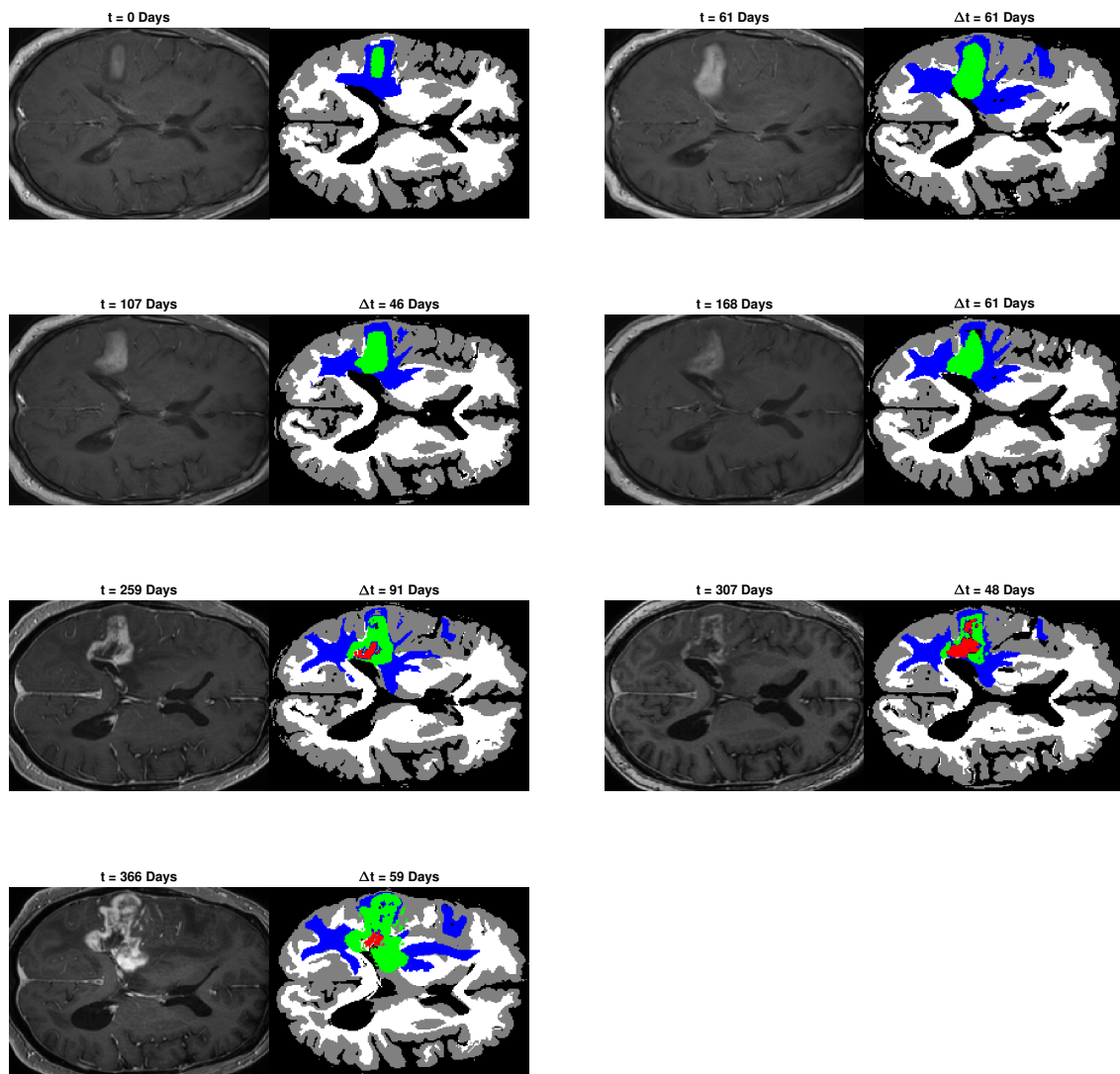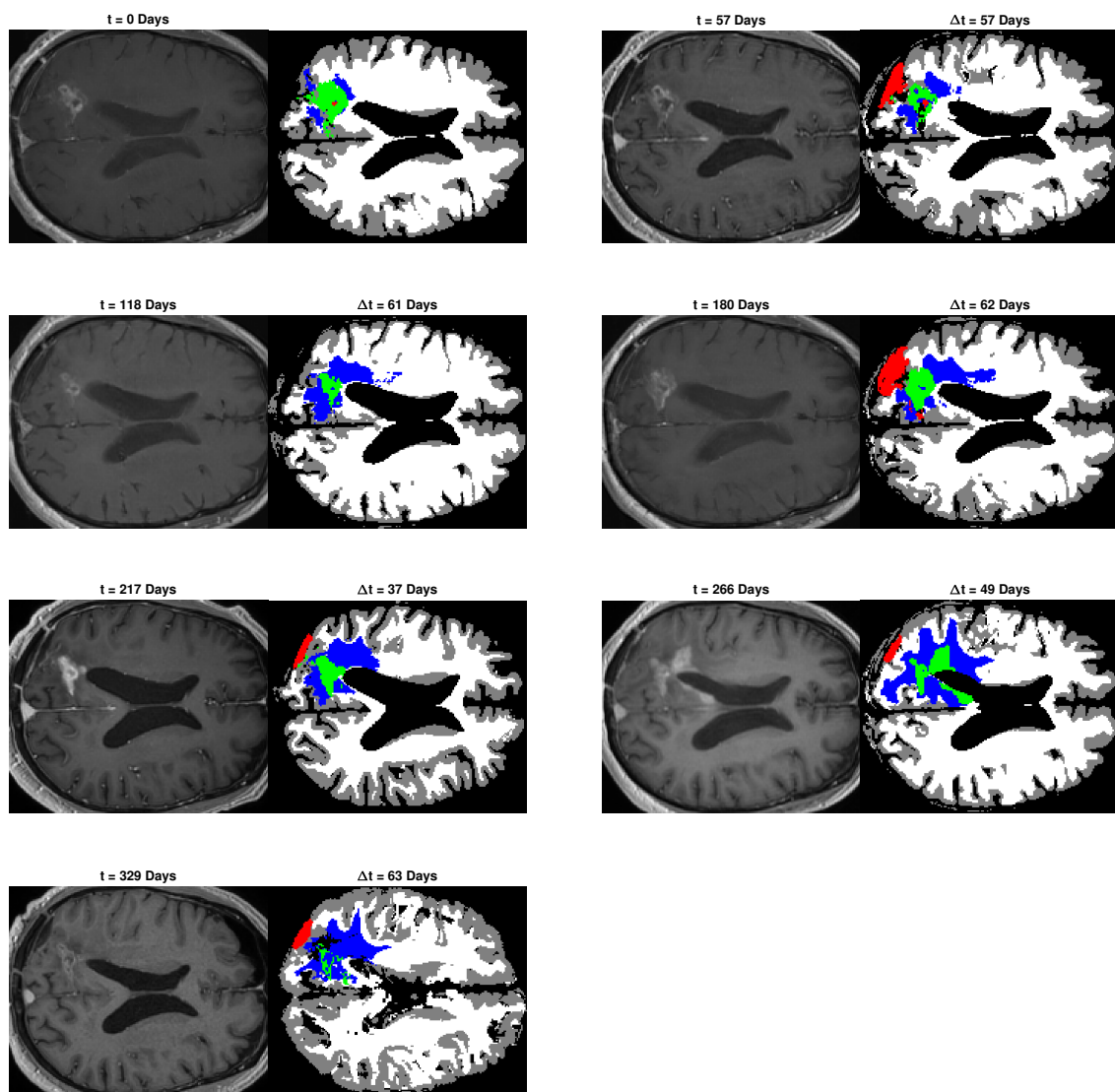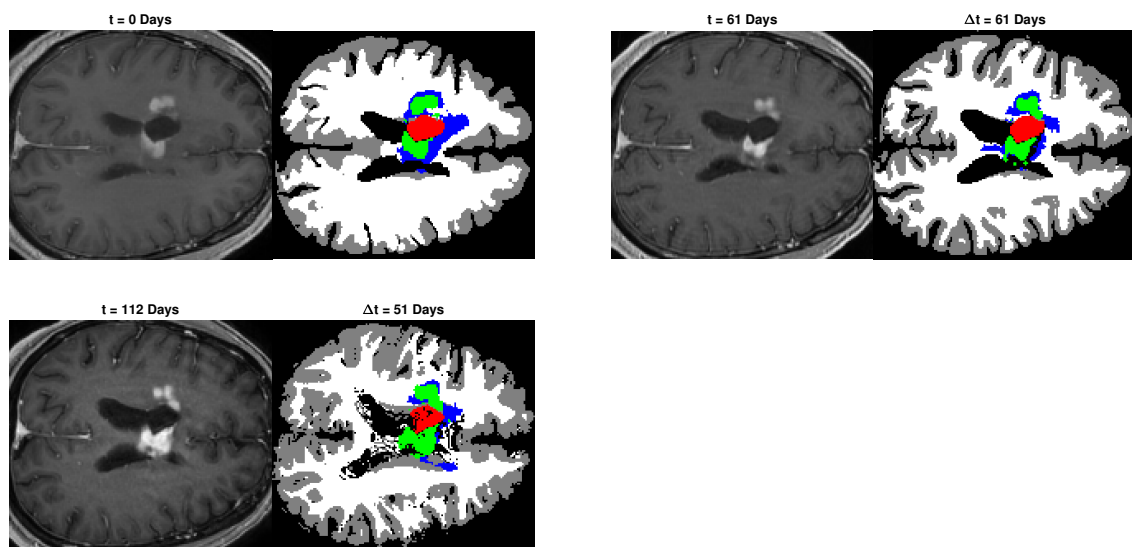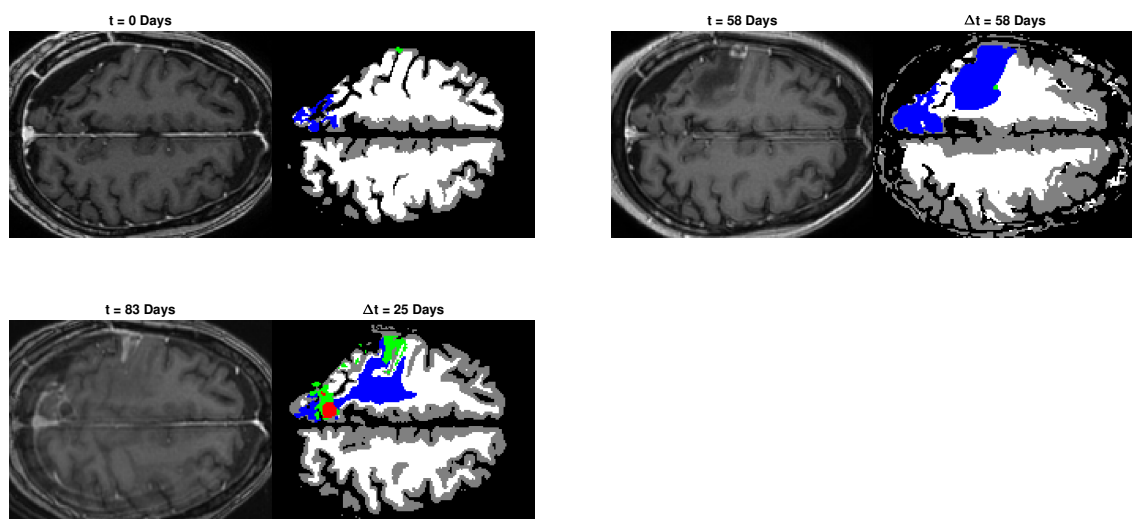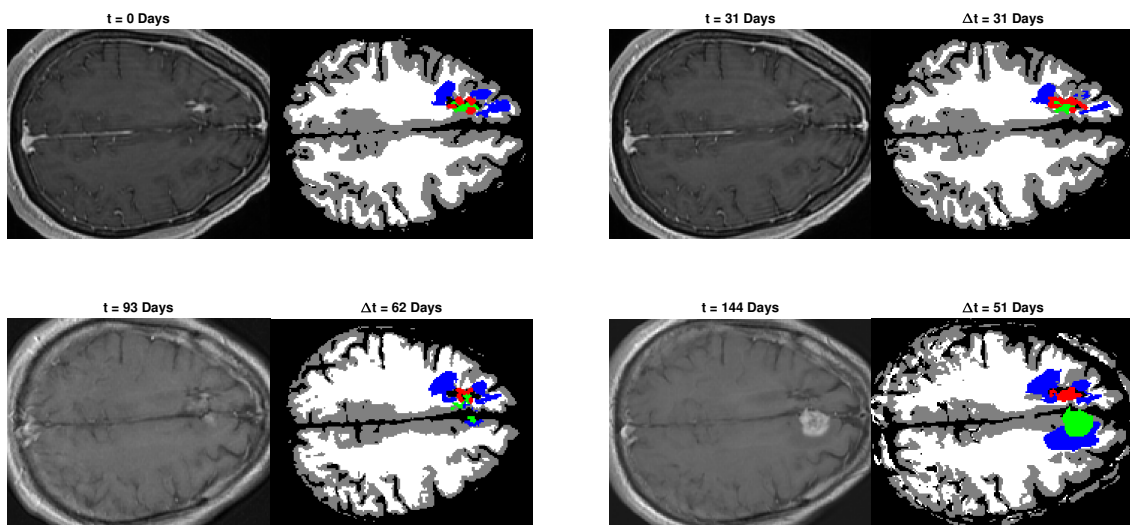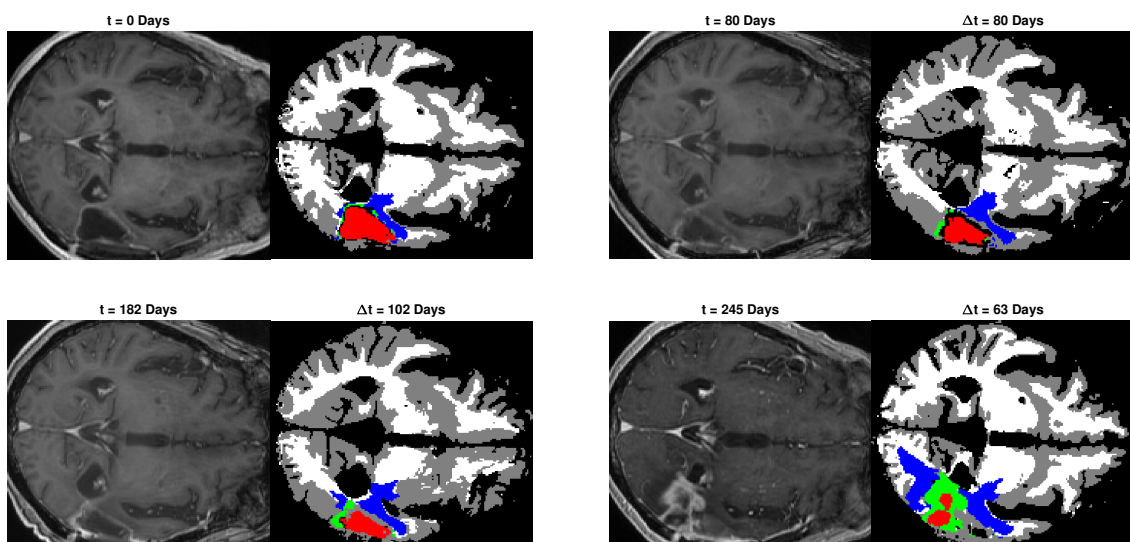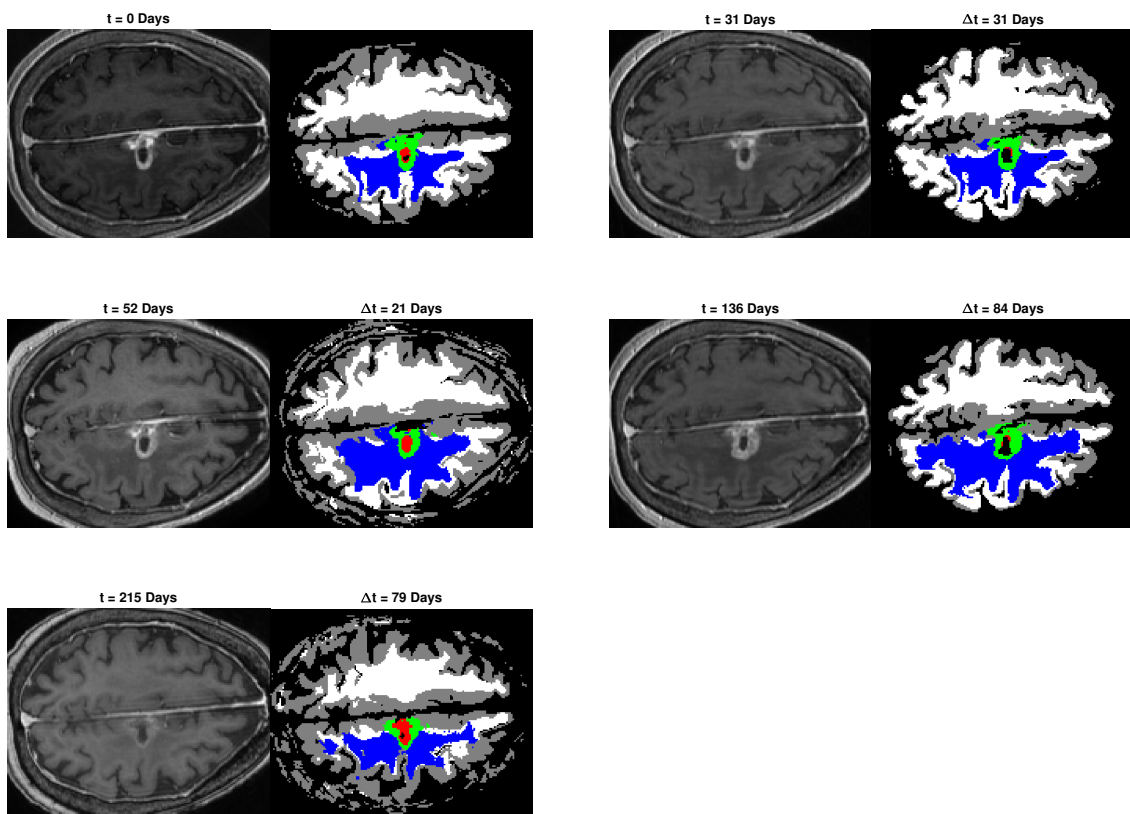
Figure S3. Representative cross-section of MRIs and tumor segmentations for patient 4 at all time points. The panels are as in Figure 2.

Figure S4. Representative cross-section of MRIs and tumor segmentations for patient 5 at all time points. The panels are as in Figure 2.

Figure S5. Representative cross-section of MRIs and tumor segmentations for patient 6 at all time points. The panels are as in Figure 2.

Figure S6. Representative cross-section of MRIs and tumor segmentations for patient 7 at all time points. The panels are as in Figure 2.

Figure S7. Representative cross-section of MRIs and tumor segmentations for patient 8 at all time points. The panels are as in Figure 2.

Figure S8. Representative cross-section of MRIs and tumor segmentations for patient 9 at all time points. The panels are as in Figure 2.

Figure S9. Representative cross-section of MRIs and tumor segmentations for patient 10 at all time points. The panels are as in Figure 2.

Ensemble results
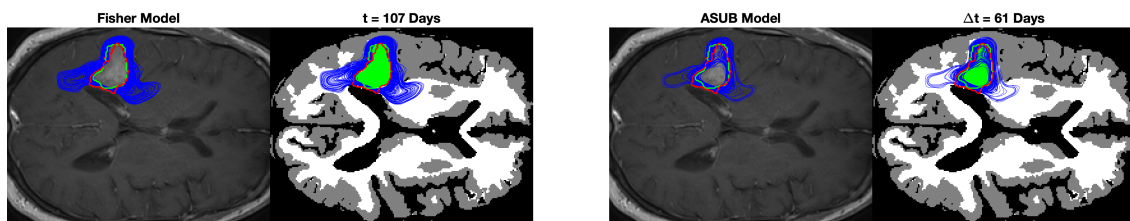
Figure S10. Ensemble simulations for Patient 4. The panels are as in Figure 3.
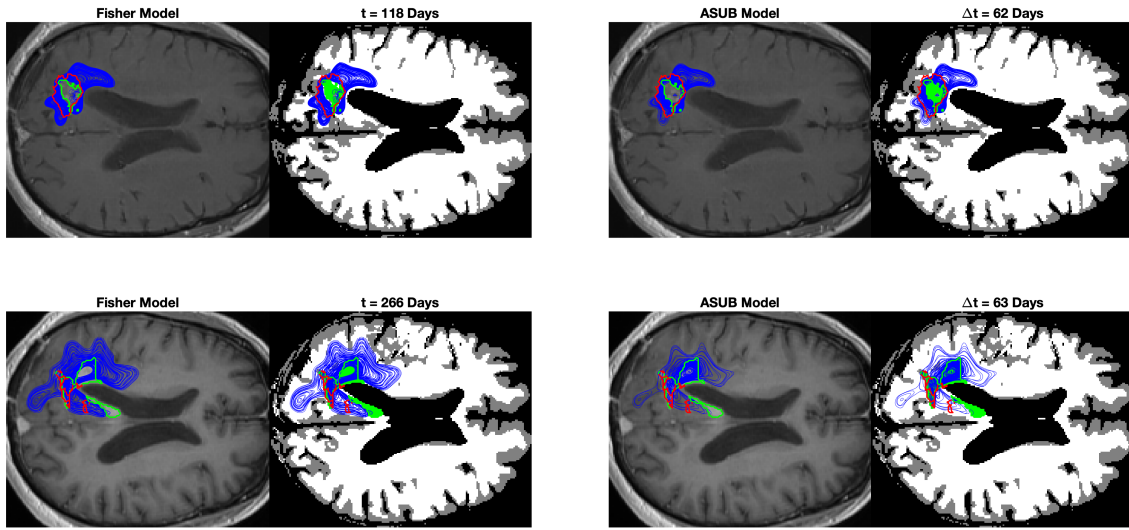
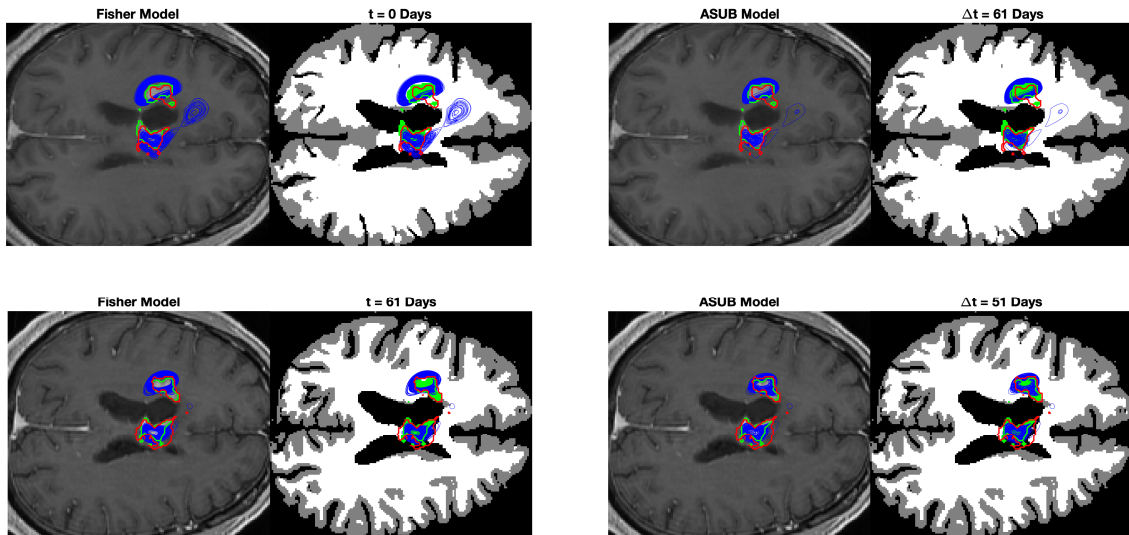**Figure S11.** Ensemble simulations for Patient 5. The panels are as in Figure 3.

Figure S12. Ensemble simulations for Patient 6. The panels are as in Figure 3.
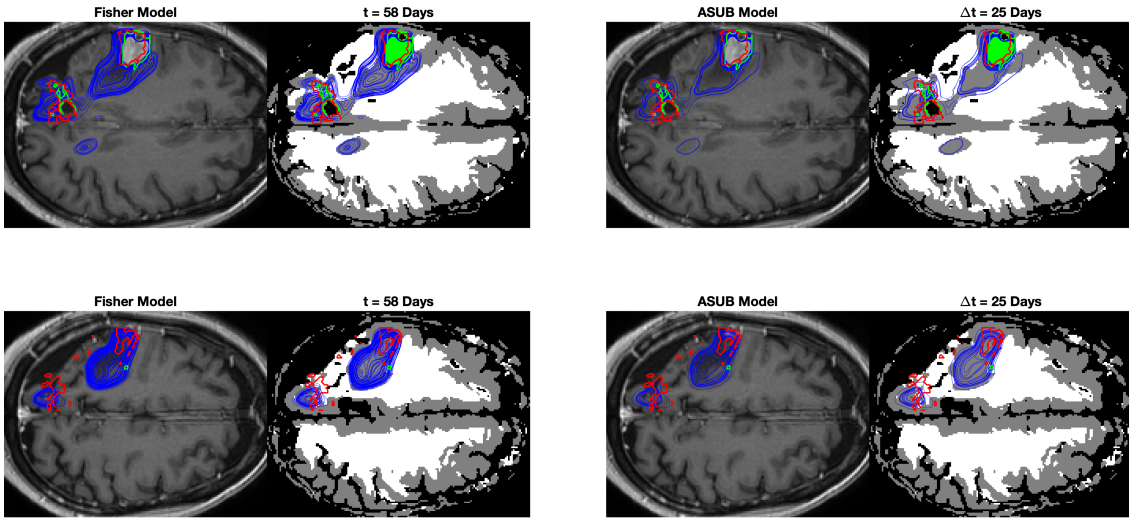
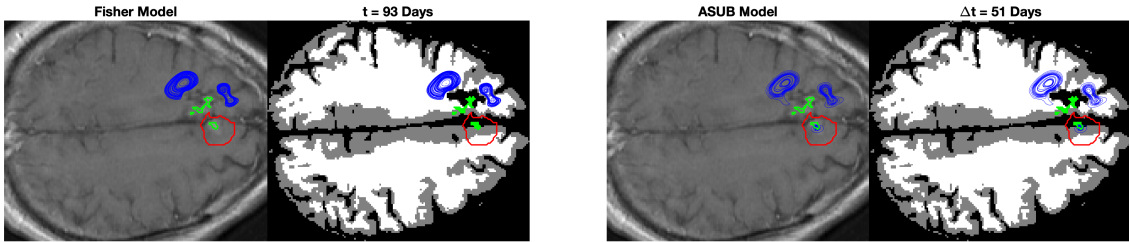**Figure S13.** Ensemble simulations for Patient 7. The panels are as in Figure 3.

Figure S14. Ensemble simulations for Patient 8. The panels are as in Figure 3.
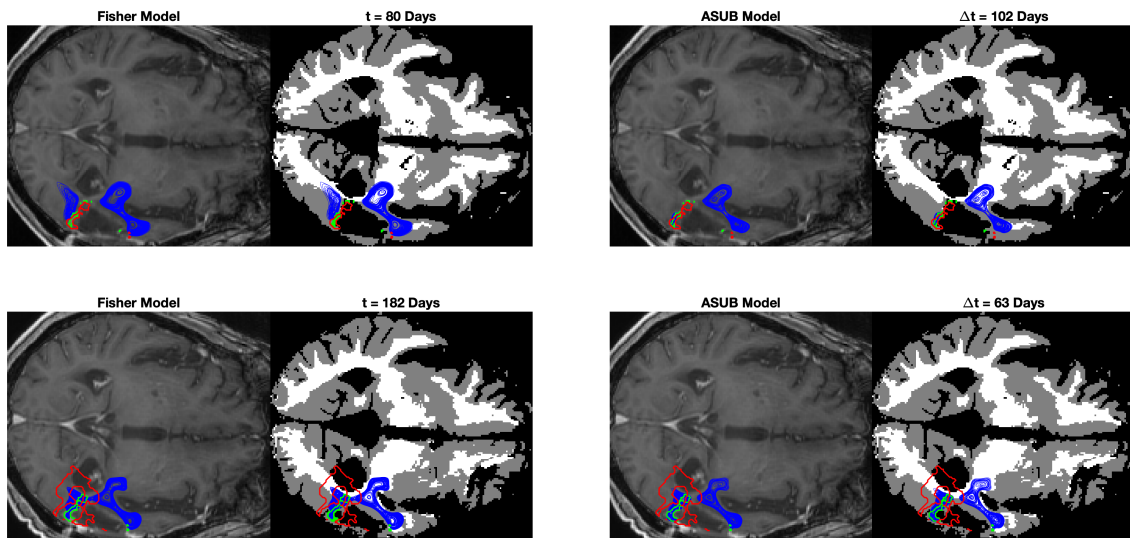
Figure S15. Ensemble simulations for Patient 9. The panels are as in Figure 3.
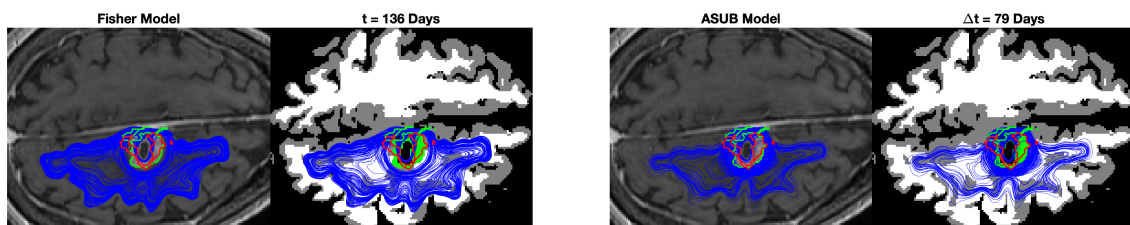

Figure S16. Ensemble simulations for Patient 10. The panels are as in Figure 3.

Containment and agreement results

Table S1. Containment

Patient/Time	Fisher				ASUB			
	Min	Max	Avg	StD	Min	Max	Avg	StD
1 / 56-114	0.18	0.41	0.28	0.05	0.08	0.38	0.25	0.06
1 / 114-142	0.16	0.45	0.23	0.04	0.14	0.53	0.23	0.05
1 / 142-168	0.31	0.85	0.39	0.09	0.27	0.86	0.38	0.07
2 / 56-158	0.06	0.64	0.43	0.15	0.02	0.57	0.26	0.17
3 / 182-238	0.22	0.48	0.35	0.06	0.12	0.44	0.27	0.08
3 / 238-266	0.11	0.33	0.18	0.05	0.11	0.41	0.22	0.06
4 / 107-168	0.56	0.76	0.66	0.05	0.29	0.76	0.58	0.10
5 / 118-180	0.09	0.21	0.17	0.03	0.06	0.20	0.13	0.03
5 / 266-329	0.31	0.52	0.38	0.05	0.22	0.48	0.33	0.04
6 / 0- 61	0.21	0.33	0.26	0.03	0.13	0.34	0.24	0.05
6 / 61-112	0.20	0.31	0.25	0.02	0.12	0.32	0.24	0.05
7 / 0- 58	0.12	0.40	0.26	0.07	0.05	0.37	0.18	0.07
7 / 58- 83	0.16	0.56	0.24	0.09	0.15	0.55	0.22	0.07
8 / 93-144	0.02	0.19	0.13	0.02	0.09	0.23	0.15	0.03
9 / 80-182	0.00	0.03	0.02	0.01	0.00	0.06	0.03	0.01
9 / 182-245	0.03	0.12	0.07	0.02	0.02	0.11	0.07	0.02
10 / 136-215	0.44	0.68	0.61	0.05	0.32	0.69	0.56	0.08

Table S2. Agreement

| Patient/Time	Fisher				ASUB			
	Min	Max	Avg	StD	Min	Max	Avg	StD
1 / 56-114	0.18	0.33	0.25	0.03	0.08	0.36	0.24	0.06
1 / 114-142	0.16	0.43	0.23	0.04	0.14	0.48	0.23	0.05
1 / 142-168	0.31	0.55	0.37	0.05	0.27	0.51	0.37	0.05
2 / 56-158	0.06	0.36	0.29	0.08	0.02	0.38	0.21	0.11
3 / 182-238	0.16	0.32	0.26	0.03	0.11	0.31	0.23	0.05
3 / 238-266	0.11	0.28	0.18	0.04	0.11	0.34	0.21	0.06
4 / 107-168	0.14	0.62	0.46	0.13	0.22	0.62	0.50	0.09
5 / 118-180	0.08	0.13	0.11	0.01	0.06	0.14	0.11	0.02
5 / 266-329	0.05	0.20	0.16	0.04	0.08	0.21	0.19	0.02
6 / 0- 61	0.09	0.26	0.18	0.04	0.12	0.29	0.20	0.03
6 / 61-112	0.11	0.26	0.21	0.03	0.12	0.27	0.20	0.04
7 / 0- 58	0.12	0.23	0.17	0.02	0.05	0.22	0.15	0.04
7 / 58- 83	0.10	0.25	0.18	0.03	0.10	0.28	0.19	0.03
8 / 93-144	0.01	0.18	0.11	0.03	0.08	0.21	0.13	0.02
9 / 80-182	0.00	0.02	0.01	0.01	0.00	0.05	0.03	0.01
9 / 182-245	0.03	0.11	0.06	0.02	0.02	0.10	0.07	0.02
10 / 136-215	0.01	0.24	0.07	0.07	0.01	0.29	0.17	0.08

Alternative ensemble results
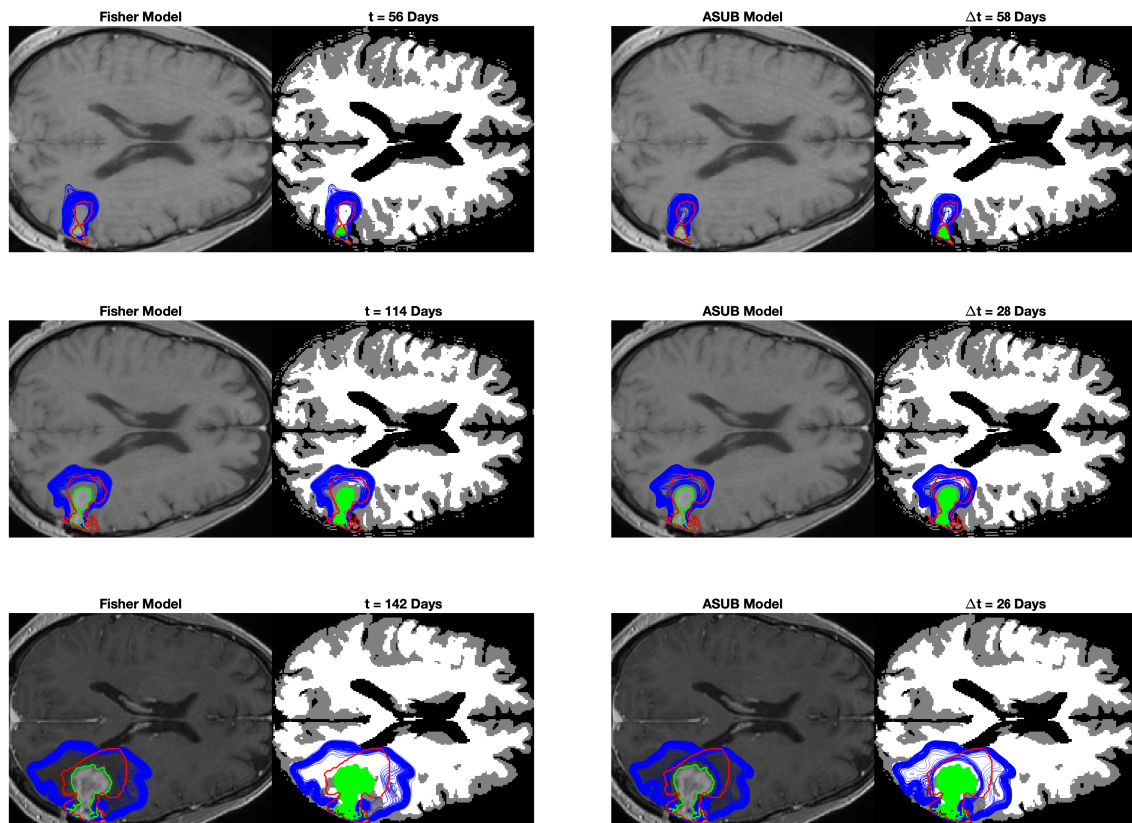
Figure S17. Alternative ensemble simulations for Patient 1. The panels are as in Figure 3.
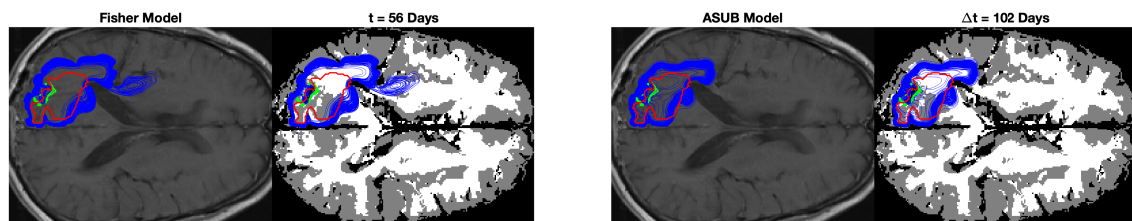

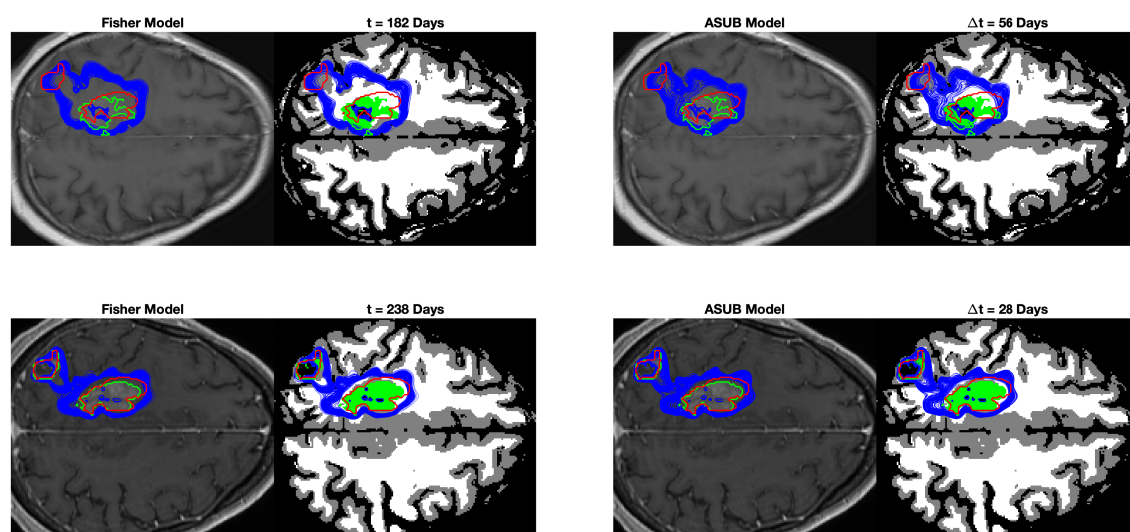**Figure S18.** Alternative ensemble simulations for Patient 2. The panels are as in Figure 3.

Figure S19. Alternative ensemble simulations for Patient 3. The panels are as in Figure 3.

AIMS Press